

Confidence Intervals for Extinction Risk: Validating Population Viability Analysis with Limited Data

Hiroshi Hakoyama¹

¹Institute of Freshwater Biology, Nagano University,
1088 Komaki, Ueda, Nagano 386-0031, Japan
hiroshi-hakoyama@nagano.ac.jp

Abstract

1. The assessment of extinction risk remains a key component of IUCN Red List and CITES evaluations. However, it has been argued that, under realistic data limitations, confidence intervals (CIs) for extinction probability often span the entire 0–1 range, rendering such assessments meaningless. I revisit the issue by analytically deriving accurate CIs under the Wiener process with drift, a canonical model of extinction dynamics.
2. In this model, extinction probability G depends on the time horizon, growth rate, environmental variance, and initial population size relative to the threshold. I define two transformed parameters, w and z , derived from the original parameters, each following a noncentral t distribution. When the initial population is far above the threshold relative to expected drift and environmental variability ($z \gg 0$), G reduces to a function of w alone, enabling exact CIs. In contrast, for $z \ll 0$, w and z are strongly negatively correlated, so I construct a CI for G by evaluating $G(w, z)$ at diagonally opposite corners of the joint confidence rectangle for (w, z) . This yields CIs with superior coverage compared to existing methods.
3. Using this approach, I quantitatively examine how the observation span of available time series affects the width of the CI for extinction probability. A key finding is that the CI width depends on both the data and the parameters, particularly on effect size, defined as the distance between the true G and the maximally uncertain midpoint ($G \simeq 0.5$). Even with limited time-series data, extinction probabilities that are sufficiently low or high can be reliably estimated, addressing a long-standing concern that population viability analysis (PVA) becomes unreliable under data scarcity.

4. Applying this method to three 64-year catch series for Japanese eel (*Anguilla japonica*) as abundance indices, I find that the extinction risk lies well below the Criterion E thresholds for Critically Endangered and Endangered, with narrow CIs. Although the species is currently listed as Endangered under Criterion A (population decline), this analysis shows that decline-based assessments substantially overestimate extinction risk in large populations.

Keywords: *Anguilla japonica*, confidence intervals, extinction probability, IUCN Red List criteria, limited data, noncentral t distribution, population viability analysis, Wiener process with drift

1 Introduction

The reliability of extinction risk assessments has been debated for several decades. In his paper *Is it meaningful to estimate a probability of extinction?*, Ludwig (1999) pointed out that when models are poorly fitted to short time series, the CI for the extinction probability becomes wide, and warned that ignoring CIs in extinction risk assessments may lead to over-optimism. Building on this concern, Fieberg & Ellner (2000) investigated whether the extinction probability could be estimated with meaningful precision despite data limitations. They concluded that accurate long-term predictions of extinction risk would require unrealistically long monitoring periods. Using analyses based on diffusion approximations, they found that reliable estimates are possible only over short-term time horizons, typically 10–20% of the monitoring period. If this assertion were correct, then reliably estimating extinction risk over a century, as required by IUCN Criterion E for Vulnerable species, for example, would require centuries of monitoring, which is impractical.

While these theoretical concerns emphasize limitations in estimating extinction risk, empirical evidence offers a more optimistic view. Brook *et al.* (2000) tested PVA retrospectively on 21 long-monitored populations and found that model projections closely matched subsequent observations. These results underscore the practical value of PVA for conservation. Ellner *et al.* (2002), however, argued that, although PVA predictions appeared essentially unbiased when averaged across the ensemble of 21 species, the CIs for individual species remained so wide, especially when data were limited, that practical precision was lacking. Brook *et al.* (2002) replied that, despite this limitation, PVA remains the most transparent quantitative tool available.

A different perspective was introduced by Halley (2003), who proposed that long-term trends or drift in model parameters, which are characteristic of reddened environmental variability, could actually improve the precision of extinction risk quantification. This suggestion runs counter to earlier concerns about the high sensitivity of extinction risk to small differences in growth rate. Halley argued that such drift weakens the dependence of extinction risk on growth rate and instead shifts it to other parameters, such as environmental variance, for which estimates may be less sensitive. In

contrast, Ellner (2003) critiqued this view by pointing out that although drift may mitigate sensitivity to growth rate, it also increases uncertainty in the parameter estimates themselves, particularly when the available data are limited.

Simulation studies have provided further support for the feasibility of estimating extinction risk with limited data. Holmes *et al.* (2007) examined CIs derived from parametric bootstrap simulations of a simple extinction model, using 63 time series, each at least 30 years long. Their simulations showed that 20–30-year time series can yield estimates with 95 % CIs that are substantially narrower than the full 0–1 range, particularly for declining populations and those exhibiting rapid fluctuations. The authors further argued that forecasting a population’s extinction risk does not necessarily require knowledge of population structure, as the stochastic nature of population growth means that population trajectories across various processes can often be described by a common stochastic model. Previous work likewise demonstrates that structured models can often be approximated by simple diffusions; age-structured populations (Lande & Orzack, 1988) and metapopulations (Hakoyama & Iwasa, 2005) are notable examples. Ellner & Holmes (2008) reconciled the relatively narrow 95 % CIs for many vertebrate populations reported by Holmes *et al.* (2007) with earlier theoretical predictions of much wider intervals (Fieberg & Ellner, 2000). By analytically mapping combinations of the time horizon and the initial distance to the extinction threshold, they identified when high precision can be achieved, albeit under the strong assumption that the growth rate is the sole estimated parameter and the environmental variance is fixed. These analytical results provide initial insight into when high precision is attainable, although they do not explore how CI width varies with the risk itself.

Despite these advances, the statistical methods for estimating CIs for extinction probability are often inadequate in terms of coverage. Approaches for constructing CIs, including the delta/logit method (e.g., Dennis *et al.*, 1991), the percentile form of the parametric bootstrap (e.g., Efron & Tibshirani, 1993), and methods that ignore variance uncertainty (Ellner & Holmes, 2008), often deliver poor coverage. Holmes *et al.* (2007) also used a parametric bootstrap approach, although the details of their CI construction are not fully described, making it difficult to evaluate the coverage properties of their approach. From a statistical perspective, a CI is the inverse of a hypothesis test, and its width is governed by both sample size and effect size, that is, a function of the parameters that quantifies the magnitude of a phenomenon (e.g., Cohen, 1988). The key question is therefore not simply how many data points are needed, but which model quantities serve as effect sizes and, for each such effect size, how much data are required to attain a desired level of confidence. In extinction models, I examine the possibility that a function of the extinction probability serves as an effect size: when risks are very high or very low, the parameter deviates strongly from its null value, permitting narrow CIs, as illustrated in Holmes *et al.* (2007, Fig. 8e). Here, I derive an analytical CI with near-nominal coverage for the extinction probability under the Wiener process with drift, explicitly incorporating the effect size perspective to clarify when reliable estimation is feasible with limited data. I then apply the method to assess the extinction risk of the Japanese eel (*Anguilla japonica*).

2 Materials and Methods

I quantify extinction risk under a Wiener process with drift using the w - z method (see Section 4) and construct CIs as developed in the main text and in the Supporting Information (Appendices). Numerical calculations were performed in R (version 4.5.1) with standard libraries. I used a large language model to assist with code refactoring and phrasing: ChatGPT (OpenAI, GPT-5 Thinking; accessed Aug–Sep 2025). I reviewed and verified all AI-influenced text and code and assume full responsibility for their accuracy and legality. No copyrighted third-party text was incorporated, and AI-assisted code segments are annotated in the source files.

3 Model and Analytical Properties

3.1 Stochastic differential equation

Population dynamics are modeled by a stochastic differential equation that describes the change in population size $N \in (0, \infty)$ over continuous time $t \in [0, \infty)$. The equation is given by

$$dN = rN dt + \sigma N dW, \quad (1)$$

where $r \in \mathbb{R}$ is the instantaneous per-capita growth rate, and $\sigma \in (0, \infty)$ denotes the intensity of environmental stochasticity. The environmental variance is given by σ^2 . The term $W(t)$ denotes a Wiener process modeling continuous-time random fluctuations due to environmental stochasticity. The stochastic term $\sigma N dW$ is interpreted in the Itô sense, which results in different long-term behavior from the Stratonovich interpretation (see e.g., Hakoyama & Iwasa, 2000). This model does not account for density dependence, and is therefore more appropriate for non-stationary populations (those expected to grow or decline) than for populations near equilibrium, for which density-dependent models are preferable (e.g., Hakoyama & Iwasa, 2000).

To facilitate analysis on a log scale, the natural logarithm of the population size is taken, $X = \log N$ (log hereafter means \ln). Applying Itô's lemma to Eq. (1) yields the following simplified equation, which describes a Wiener process with drift:

$$dX = \mu dt + \sigma dW, \quad (2)$$

where $\mu = r - \frac{1}{2}\sigma^2$ is the drift parameter. Eq. (2) has been extensively used as a simple extinction model (e.g., Lande & Orzack, 1988; Dennis *et al.*, 1991).

Equations (1) and (2) represent the same stochastic process, expressed on the absolute scale (a geometric Brownian motion) and on the log scale (a Wiener process with drift), respectively. The expectations of these processes evolve as follows:

$$\mathbb{E}[N(t)] = n_0 e^{rt}, \quad \mathbb{E}[X(t)] = x_0 + \mu t,$$

where n_0 and $x_0 = \log n_0$ are the initial population sizes on the absolute and log scales, respectively. Thus, r represents the long-run average growth rate on the absolute scale (actual population numbers), whereas μ represents the corresponding rate on the log scale.

In applications, the growth rate r estimated from time-series data reflects both the intrinsic biological potential of the population and external influences such as fishing pressure, pollution, disease transmission, and other anthropogenic or environmental factors.

3.2 Extinction probability

In practice, extinction is typically defined not as the population reaching exactly zero, but as falling below a small, biologically meaningful threshold (e.g., $n_e = 1$, representing a single individual). This is because, under Eq. (1), true extinction ($N = 0$) is theoretically unreachable: although $N(t)$ may asymptotically approach zero due to stochastic fluctuations, the noise term $\sigma N dW$ diminishes proportionally with population size, preventing extinction from occurring in finite time. Under this definition, extinction is said to occur when the population size $N(t)$ falls at or below a threshold n_e , corresponding to $X(t) \leq \log(n_e)$ on the log scale.

Let $T \in [0, \infty]$ be the random variable representing the (possibly infinite) first-passage time at which the population size, starting from an initial value n_0 , reaches a lower extinction threshold n_e . The probability that extinction occurs by time $t > 0$, given the growth rate $\mu \in \mathbb{R}$, environmental variance $\sigma^2 > 0$, and initial log-distance $x_d = \log(n_0/n_e) > 0$, is given by

$$\Pr[T \leq t] = G(t | x_d, \mu, \sigma^2) = \Phi\left(\frac{-\mu t - x_d}{\sigma\sqrt{t}}\right) + \exp\left(\frac{-2\mu x_d}{\sigma^2}\right) \Phi\left(\frac{\mu t - x_d}{\sigma\sqrt{t}}\right), \quad (3)$$

where $\Phi(\cdot)$ denotes the cumulative distribution function (CDF) of the standard normal distribution. This expression originates from classical results on first-passage times of diffusion processes (e.g., Cox & Miller, 1965) and has been applied to extinction problems in ecology (e.g., Lande & Orzack, 1988).

As shown by Lande & Orzack (1988), the ultimate extinction probability is given by

$$G(\infty | x_d, \mu, \sigma^2) = \begin{cases} 1 & \text{for } \mu \leq 0, \\ \exp\left(-\frac{2\mu x_d}{\sigma^2}\right) & \text{for } \mu > 0. \end{cases} \quad (4a)$$

That is, if the growth rate is non-positive, extinction is certain in the long run; if it is positive, the population may persist indefinitely. Accordingly, the extinction probability $G(t | x_d, \mu, \sigma^2)$ in Eq. (3) is a proper CDF for $\mu \leq 0$, but an improper one for $\mu > 0$.

The proper conditional distribution of extinction times, given that extinction eventually occurs, is obtained by dividing the unconditional extinction probability Eq. (3) by the ultimate extinction probability in Eq. (4): $\Pr[T \leq t \mid T < \infty]$ (Dennis *et al.*, 1991, Eq. (16), which contains a typographical error: in the second term inside the Φ function, the numerator should read $-x_d - |\mu|t$). This conditional distribution is the cumulative distribution function of the inverse Gaussian distribution. However, when $\mu > 0$ and the ultimate extinction probability is sufficiently small, the unconditional extinction probability $\Pr[T \leq t]$ accurately reflects the true extinction risk over time, whereas the conditional distribution $\Pr[T \leq t \mid T < \infty]$ may significantly overestimate the extinction risk. For example, with $\mu = 0.1$, $\sigma^2 = 0.1$, $n_0 = 100$, and $n_e = 1$, the unconditional extinction probability by $t = 50$ is extremely low, $G(50) = 6.6 \times 10^{-5}$, while the conditional probability among populations that eventually go extinct is much higher, $G(50)/G(\infty) = 0.66$. In other words, while nearly all populations persist, the few that happen to be destined for extinction tend to disappear quickly. For this reason, extinction risk is evaluated using the unconditional probability given by Eq. (3), which, as in Lande & Orzack (1988); Fieberg & Ellner (2000); Ellner & Holmes (2008), accurately reflects the practical extinction risk relevant to finite-time assessments, such as those used by the IUCN.

3.3 Extinction–risk landscape in transformed parameter space

As in Eq. (3), the extinction probability G depends nonlinearly on all three biological parameters (the growth rate μ , the environmental variance σ^2 , and the initial log-distance x_d) and the time horizon t . Here, μ and σ^2 have units of time^{-1} , while x_d is dimensionless. For analytical convenience and CI construction, I adopt the (w, z) transformation rather than the earlier (U, V) rescaling with $U = -\mu\sqrt{t}/\sigma$ and $V = x_d/(\sigma\sqrt{t})$ (Fieberg & Ellner, 2000; Ellner & Holmes, 2008). I then define

$$w = \frac{\mu t + x_d}{\sigma\sqrt{t}}, \quad z = \frac{-\mu t + x_d}{\sigma\sqrt{t}}. \quad (5)$$

Each variable is a signal-to-noise ratio expressed in dimensionless form: the numerator represents net deterministic displacement toward or away from the threshold, and the denominator, $\sigma\sqrt{t}$, characterizes the scale of stochastic fluctuation. This dimensionless scaling is natural in first-passage problems and quantifies expected movement relative to noise. The transformation from $(\mu t, x_d)$ to (w, z) can be interpreted geometrically as a 45° clockwise rotation, followed by isotropic scaling by $\sqrt{2}/(\sigma\sqrt{t})$:

$$\begin{pmatrix} w \\ z \end{pmatrix} = \frac{1}{\sigma\sqrt{t}} \begin{pmatrix} 1 & 1 \\ -1 & 1 \end{pmatrix} \begin{pmatrix} \mu t \\ x_d \end{pmatrix}.$$

Applying the change of variables in Eq. (5) to Eq. (3) yields a compact expression for the extinction probability:

$$G(w, z) = \Phi(-w) + \exp\left(\frac{z^2 - w^2}{2}\right) \Phi(-z) \quad \text{for } w + z > 0, \quad w, z \in \mathbb{R}, \quad (6)$$

which depends solely on the transformed coordinates (w, z) and expresses extinction probability as a function of signal-to-noise ratios. The condition $w + z > 0$ follows from $w + z = 2x_d/(\sigma\sqrt{t})$, and reflects the assumption that the initial population size n_0 exceeds the extinction threshold n_e . The introduced parameters w and z can be estimated via maximum likelihood, and their estimators have tractable sampling distributions, specifically noncentral t , as derived in subsection 4.2. This analytical tractability forms the foundation for the CI construction discussed in section 4. Numerical procedures for evaluating $G(w, z)$ are detailed in Appendix S1. $G(w, z)$ exhibits similar numerical instability in the tails as the inverse Gaussian CDF, as reported by Dennis *et al.* (1991) and Giner & Smyth (2016).

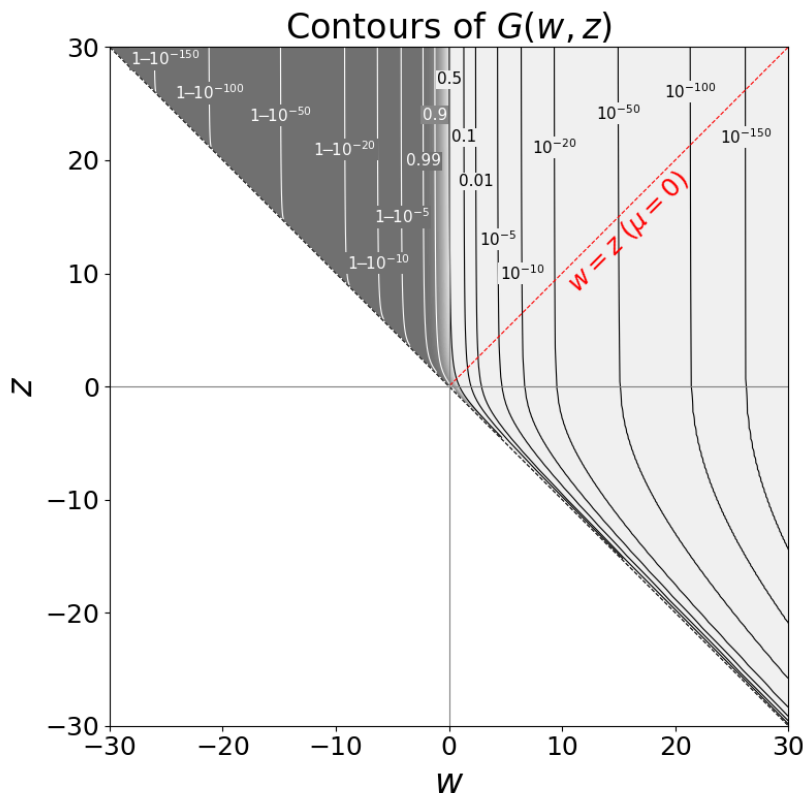


Figure 1: Contour plot of extinction probability $G(w, z)$ in the (w, z) space, restricted to $w + z > 0$. Shading indicates extinction risk (light: low, dark: high), with contours labeled by $G(w, z)$. The red dotted line ($w = z$) separates regions of positive drift ($\mu > 0$, below) and negative drift ($\mu < 0$, above).

While the function $G(w, z)$ is strictly decreasing in both arguments throughout the domain $w + z > 0$ (Appendix S2), the nature of this decline is not uniform across the domain. In the two extreme regimes within the region $w + z > 0$, one can apply the leading-order Mills ratio approximation $\Phi(-x) \sim \phi(x)/x$ as $x \rightarrow +\infty$ (with $\phi(x) =$

$\frac{1}{\sqrt{2\pi}}e^{-x^2/2}$) to obtain the following asymptotic form:

$$G(w, z) = \begin{cases} \Phi(-w) & \text{for } z \gg 0, \\ \exp\left(\frac{z^2 - w^2}{2}\right) & \text{for } z \ll 0. \end{cases} \quad (7a)$$

When $z \gg 0$, the second term in Eq. (6) becomes negligible, and extinction risk is determined primarily by w . Conversely, when $z \ll 0$, the second term $\exp((z^2 - w^2)/2)[1 + o(1)]$ dominates; hence $w^2 - z^2 = \text{const}$ along contours of constant $G(w, z)$. Along such contours in $z \ll 0$, the derivative satisfies $dw/dz = z/w \rightarrow -1$, indicating that extinction risk is most sensitive to changes along the diagonal direction $z \approx -w$. This asymmetry reflects the distinct ways in which drift and stochasticity interact to shape extinction risk. See Appendix S3 for a derivation of this asymptotic behavior. Notably, the expression $\exp((z^2 - w^2)/2)$ for $z \ll 0$ (i.e., for $\mu > 0$ with $\mu t \gg x_d$) is identical to the ultimate extinction probability $\exp(-2\mu x_d/\sigma^2)$ derived by Lande & Orzack (1988, Eq. 4b).

Fig. 1 shows that the equal-risk contours are nearly vertical over a broad range of positive z values ($z > 0$; equivalently, $x_d > \mu t$), indicating that the extinction probability is primarily governed by horizontal variation in w . This confirms that the approximation $G(w, z) \simeq \Phi(-w)$ holds well in this region. In contrast, in the lower-right portion of the plotted domain ($z < 0$; equivalently, $x_d < \mu t$), the contours are oriented approximately along the line $z \approx -w$, indicating increased sensitivity to coordinated changes in both w and z . This pattern aligns with the asymptotic structure derived in Appendix S3, where both limiting expressions achieve relative accuracy of $O(|z|^{-2})$ (see the Remark there). Such second-order accuracy supports their use in the construction and interpretation of CIs. As evident in Fig. 1, the equal-risk contours are steeper than the diagonal $w = -z$ throughout $w + z > 0$, and their slopes approach -1 from below as $z \rightarrow -\infty$, consistent with the analytical result $dz/dw < -1$ on $w + z > 0$ proved in Appendix S4.

4 Estimation and Confidence Intervals

To quantify extinction risk from time-series data, I derive estimators for the parameters of the diffusion model and construct CIs for the finite-horizon extinction probability. The analysis is based on maximum likelihood (ML) estimation and rescaled coordinates that lead to a tractable sampling distribution. This section develops the estimation procedure, derives the associated sampling laws, and describes a method for constructing CIs without linear approximation.

4.1 Maximum likelihood estimation of μ and σ^2

Let $\mathbf{n}_{\text{obs}} = \{n_{t_0}, n_{t_1}, \dots, n_{t_q}\}$ be a univariate time series observed at unequally spaced times $t_0 = 0 < t_1 < \dots < t_q$, arising from the stochastic process in Eq. (1). Define the

log-transformed values $x_i = \log n_{t_i}$ and denote the sampling intervals by $\tau_i = t_i - t_{i-1} > 0$. Under model (2), the log-increments are independent and satisfy

$$x_i - x_{i-1} \sim \mathcal{N}(\mu \tau_i, \sigma^2 \tau_i) \quad \text{for } i = 1, \dots, q.$$

Here q denotes the number of increments (so the sample size of the series is $q + 1$), and t_q is the length of the observation span.

The Gaussian likelihood based on these increments leads to the ML estimators (Dennis *et al.*, 1991, Eqs. (24)–(26))

$$\hat{\mu} = \frac{\sum_{i=1}^q (x_i - x_{i-1})}{\sum_{i=1}^q \tau_i} = \frac{x_q - x_0}{t_q}, \quad \hat{\sigma}^2 = \frac{1}{q} \sum_{i=1}^q \frac{(x_i - x_{i-1} - \hat{\mu} \tau_i)^2}{\tau_i}. \quad (8)$$

The estimator $\hat{\sigma}^2$ is biased downward; an unbiased alternative is

$$\tilde{\sigma}^2 = \frac{q}{q-1} \hat{\sigma}^2, \quad q > 1. \quad (9)$$

The sampling distributions of the estimators follow from standard arguments:

$$\hat{\mu} \sim \mathcal{N}\left(\mu, \frac{\sigma^2}{t_q}\right), \quad \frac{q \hat{\sigma}^2}{\sigma^2} \sim \chi_{q-1}^2, \quad q > 1, \quad (10)$$

with $\hat{\mu}$ and $\hat{\sigma}^2$ mutually independent, a property unique to the normal distribution (Geary, 1936).

4.2 Sampling distributions of the rescaled statistics \hat{w} and \hat{z}

Applying the transformation in Eq. (5) with $t = t^*$, the finite time horizon for extinction risk prediction, to the ML estimators in Eq. (8) yields

$$\hat{w} = \frac{\hat{\mu} t^* + x_d}{\hat{\sigma} \sqrt{t^*}}, \quad \hat{z} = \frac{-\hat{\mu} t^* + x_d}{\hat{\sigma} \sqrt{t^*}}, \quad q > 1. \quad (11)$$

Since $\hat{\mu}$ is normally distributed, $\hat{\sigma}^2$ is scaled- χ^2 , and the two are independent, each follows a noncentral t distribution with $q - 1$ degrees of freedom ($q > 1$):

$$\hat{w} \sqrt{\frac{q-1}{q}} \sqrt{\frac{t_q}{t^*}} \sim t(\delta_w, q-1), \quad \hat{z} \sqrt{\frac{q-1}{q}} \sqrt{\frac{t_q}{t^*}} \sim t(\delta_z, q-1), \quad (12)$$

where the noncentrality parameters are

$$\delta_w = w \sqrt{\frac{t_q}{t^*}}, \quad \delta_z = z \sqrt{\frac{t_q}{t^*}}. \quad (13)$$

4.3 Correlation between \hat{w} and \hat{z}

To construct reliable CIs for $G(w, z)$ it is necessary to understand how the estimators \hat{w} and \hat{z} vary together. This joint behavior is described by their covariance matrix, but it can be summarized more compactly through a closed-form expression of the correlation coefficient after some algebra (see Appendix S5):

$$\rho(w, z, k) := \text{Corr}(\hat{w}, \hat{z}) = \frac{-k + wz}{\sqrt{(k + w^2)(k + z^2)}}, \quad w + z > 0, k > 0. \quad (14)$$

where

$$k = \frac{t^*/t_q}{1 - \frac{1}{2}(q-3) \{\Gamma[(q-2)/2] / \Gamma[(q-1)/2]\}^2} \approx \frac{2qt^*}{t_q}, \quad (q \text{ moderately large}). \quad (15)$$

Here k depends only on (q, t_q, t^*) and is strictly positive for $q > 3$.

Equation (14) reveals a simple geometry within the admissible region $w + z > 0$. In the first quadrant ($w, z > 0$), the sign changes along the hyperbola $wz = k$: inside this curve ($wz < k$) the correlation is negative, while outside ($wz > k$) it becomes positive. In the second and fourth quadrants ($wz \leq 0$) the correlation is negative throughout. As $|w|$ and $|z|$ grow large within $w + z > 0$, the magnitude of the correlation approaches one, with the sign determined by wz . In particular, for $z < 0$ the correlation is strongly negative; this feature is exploited later when constructing CIs for $G(w, z)$. Fig. 2 illustrates the analytic structure implied by Eq. (14).

The constant k increases with the number of increments q and time horizon t^* , and decreases with observation span t_q . Because k appears only through the combination $wz = k$ in the numerator of Eq. (14), larger values of k move the zero-correlation curve closer to the origin, shrinking the region of positive correlation in the first quadrant and strengthening the negative correlation elsewhere. These effects are quantified analytically in Appendix S5.

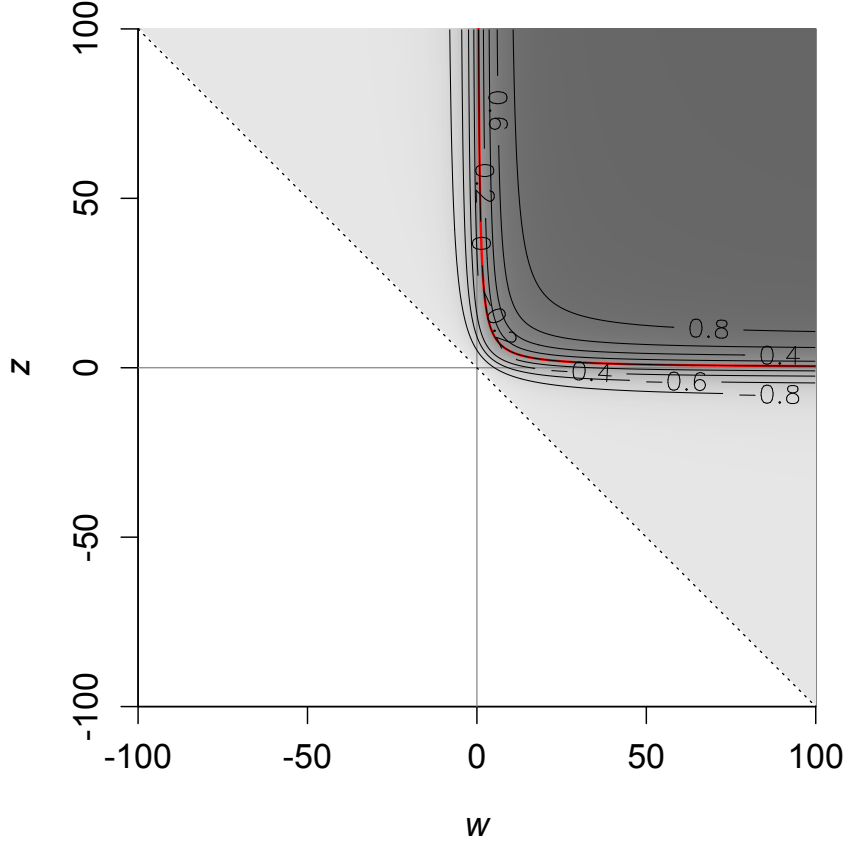


Figure 2: Correlation landscape of $\text{Corr}(\hat{w}, \hat{z})$ over the (w, z) plane, evaluated for $q = t_q = 63$ and $t^* = 25$. The red curve shows the zero-correlation hyperbola $wz = k$, where $k \approx 47.82$ as given by Eq. (15). Contours indicate correlation levels from negative (light gray) to positive (dark gray), in agreement with Eq. (14).

4.4 Confidence intervals for w and z

Let $\mathbf{N} = \{N_{t_0}, \dots, N_{t_q}\}$ be the random vector of observations from Eq. (1), and \mathbf{n}_{obs} its realization. An equal-tailed $(1 - \alpha) \times 100\%$ CI (\underline{w}, \bar{w}) for w is defined by

$$\Pr(w \leq \underline{w}(\mathbf{N})) = \Pr(w \geq \bar{w}(\mathbf{N})) = \alpha/2.$$

Equivalently, in terms of the observed estimator $\hat{w}(\mathbf{n}_{\text{obs}})$,

$$\begin{aligned} \Pr(\hat{w}(\mathbf{N}) \geq \hat{w}(\mathbf{n}_{\text{obs}}) \mid w = \underline{w}(\mathbf{n}_{\text{obs}})) &= \alpha/2, \\ \Pr(\hat{w}(\mathbf{N}) \leq \hat{w}(\mathbf{n}_{\text{obs}}) \mid w = \bar{w}(\mathbf{n}_{\text{obs}})) &= \alpha/2, \end{aligned} \tag{16}$$

because $\hat{w}(\mathbf{N})$ is monotone increasing in w .

Using the noncentral- t distribution (Eqs. (11)–(13)), let

$$t_{\text{obs}} = \widehat{w}(\mathbf{n}_{\text{obs}}) \sqrt{\frac{q-1}{q}} \sqrt{\frac{t_q}{t^*}},$$

and denote the noncentrality parameter for a given w by δ . The bounds $\underline{\delta}_{\text{obs}}, \bar{\delta}_{\text{obs}}$ solve

$$\Pr(T \geq t_{\text{obs}} \mid \delta = \underline{\delta}_{\text{obs}}) = \alpha/2, \quad \Pr(T \leq t_{\text{obs}} \mid \delta = \bar{\delta}_{\text{obs}}) = \alpha/2,$$

with $T \sim t(\delta, q-1)$. Since the noncentral- t CDF is strictly increasing in δ , the solutions are unique, and the bounds for w follow as

$$\underline{w} = \underline{\delta}_{\text{obs}} \sqrt{\frac{t^*}{t_q}}, \quad \bar{w} = \bar{\delta}_{\text{obs}} \sqrt{\frac{t^*}{t_q}}.$$

The CI for z is constructed analogously.

4.5 Confidence intervals for the extinction probability G

A $(1 - \alpha) \times 100\%$ confidence interval for $G = G(w, z)$ is defined as

$$\text{CI}_G = \left(G(\bar{w}, \underline{z}), G(\underline{w}, \bar{z}) \right),$$

hereafter referred to as the w - z method. The rationale, based on the monotonicity of G and the geometry of the joint distribution of $(\widehat{w}, \widehat{z})$, is explained below.

Simplification for large z . When z is sufficiently large, the exponential term in Eq. (6) becomes negligible, and $G(w, z)$ is well approximated by $\Phi(-w)$. The CI then simplifies to

$$\text{CI}_G = \left(\Phi(-\bar{w}), \Phi(-\underline{w}) \right),$$

which avoids the need for evaluating exponentials and, in the regime $z \gg 0$, is exact.

Justification for small z . When $z \ll 0$, the second term in Eq. (6) dominates, and the equal-risk contours of G have slope strictly less than -1 throughout the region $w + z > 0$ (Appendix S4). The joint confidence region for $(\widehat{w}, \widehat{z})$ is elongated along a direction close to slope -1 , due to strong negative correlation (see Section 4.3). In this case, evaluating G at the diagonally opposite corners (\bar{w}, \underline{z}) and (\underline{w}, \bar{z}) captures the range of variation in G over the confidence rectangle with high accuracy (see Fig. 3).

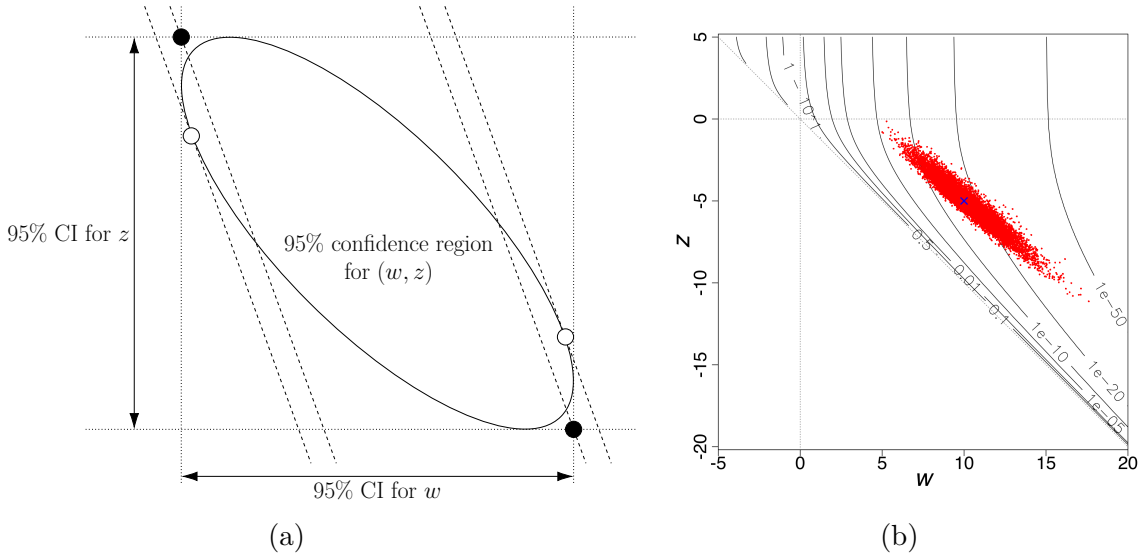


Figure 3: Geometry underlying the w - z method when $z < 0$. (a) Conceptual illustration of the joint confidence region for (w, z) when $z \ll 0$. The extinction probability $G(w, z)$ is shown as contour lines, each representing a level set. The shaded ellipse represents the joint confidence region of the estimators (\hat{w}, \hat{z}) , typically elongated along slope -1 due to negative correlation. As shown analytically in Appendix S4, the contours of G have slope strictly less than -1 , implying that they are steeper than the ellipse orientation. Black dots indicate the two diagonally opposite corners used in the w - z method. The white dot shows the point where the confidence ellipse is tangent to a G contour, yielding the exact confidence bound for G . (b) Monte Carlo sample cloud of (\hat{w}, \hat{z}) for $(w, z) = (10, -5)$, overlaid on G contours. $q = t_q = 63$ and $t^* = 100$. Although not a true confidence region, this bootstrap-type scatter plot approximately reflects the joint confidence region for (w, z) .

Implementation. The w - z method for the extinction risk assessment is implemented in the accompanying R package `extr`, available at github.com/hakoyamah/extr. It offers computationally efficient and robust estimation.

4.6 Monte Carlo validation of confidence interval accuracy

I conducted extensive Monte Carlo simulations to evaluate the accuracy of the proposed CI method for the extinction probability $G(w, z)$. For each of the 2,688 parameter combinations, 10,000 replicate time series were generated, and the empirical rejection rate (i.e., one minus the coverage probability) was computed as the proportion of intervals failing to cover the true value of G . The w - z method consistently achieved rejection rates very close to the nominal level $\alpha = 0.05$, with mean 0.053 (s.d. 0.0045, range 0.044–0.076), demonstrating accurate coverage across the full parameter range. In contrast, the delta/logit method was unstable, with rejection rates deviating widely across parameter regimes, particularly in the tails where G is near 0 or 1

(mean 0.085, s.d. 0.14, range 0.0002–1.00). The percentile bootstrap was systematically anti-conservative (mean 0.090, s.d. 0.036, range 0.049–0.20), and the theoretical minimum uncertainty (TMU) CI (Fieberg & Ellner, 2000; Ellner & Holmes, 2008) was strongly anti-conservative (mean 0.27, s.d. 0.23, range 0.050–0.84). Further details of the simulation design are provided in Appendix S6.

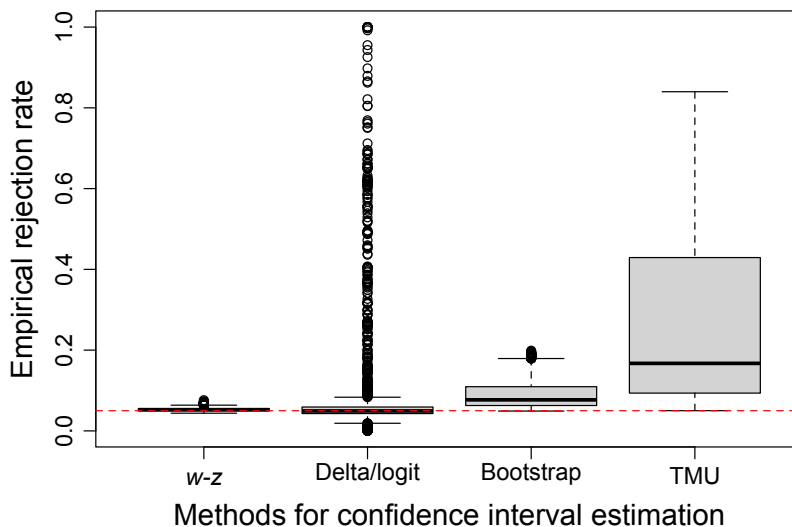


Figure 4: Empirical rejection rates of CI methods, based on Monte Carlo simulations over 2,688 parameter combinations. Each point shows the proportion of 10,000 replicates in which the true extinction probability $G(w, z)$ fell outside the estimated interval. Parameters were varied over $\mu \in \{-0.5, -0.3, -0.1, 0, 0.1, 0.3, 0.5\}$, $\sigma^2 \in \{0.001, 0.01, 0.1, 1\}$, $x_d \in \{3, 5, 7, 9, 11, 13\}$, $t^* \in \{10, 20, 50, 100\}$, and number of increments $q \in \{10, 20, 50, 100\}$. The dashed red line represents the nominal significance level $\alpha = 0.05$. Among the methods compared, the w - z interval maintains rejection rates consistently close to the nominal level, the delta/logit method deviates in both directions depending on the parameter regime, and the percentile bootstrap and TMU are predominantly anti-conservative.

4.7 Precision of extinction risk estimation: dependence on model parameters and data

The CI width for the extinction probability G depends systematically on both the model parameters and the data characteristics. As a function of G , the CI width necessarily vanishes at the boundaries $G = 0$ and $G = 1$ because $\nabla G(w, z) \rightarrow 0$ in these limits and the variances at the boundaries are zero. Since the CI width varies continuously with G , there must be at least one interior maximum (or a short plateau) between these two boundaries.

4.7.1 Dependence on model parameters

Consistent with these constraints, Fig. 5 shows a marked contrast between the positive- z case ($z = 20$) and the negative- z case ($z = -5$). For $z = 20$, the CI width is maximized near $G \simeq 0.5$ in the typical regime $k \geq 1$; as t^*/t_q increases the peak broadens and the width becomes nearly flat across intermediate G , rendering the interval informative mainly near the boundaries. For $z = -5$, the CI width is clearly unimodal with the peak around $G \simeq 0.3$ – 0.4 , and even at the peak it remains comparatively small (about 0.3–0.4). A minor exception occurs when $0 < k < 1$ for moderate $z > 0$, where the interior maximizer splits into two close peaks (cf. Fig. S7.1 c); no such split is seen for $z < 0$ (Fig. S7.1 d). Numerical calculations using the exact mixture representation confirm these patterns (Appendix S7). In practice, however, $k = q(t^*/t_q)$ is usually ≥ 1 , so the two-peak case is rarely encountered.

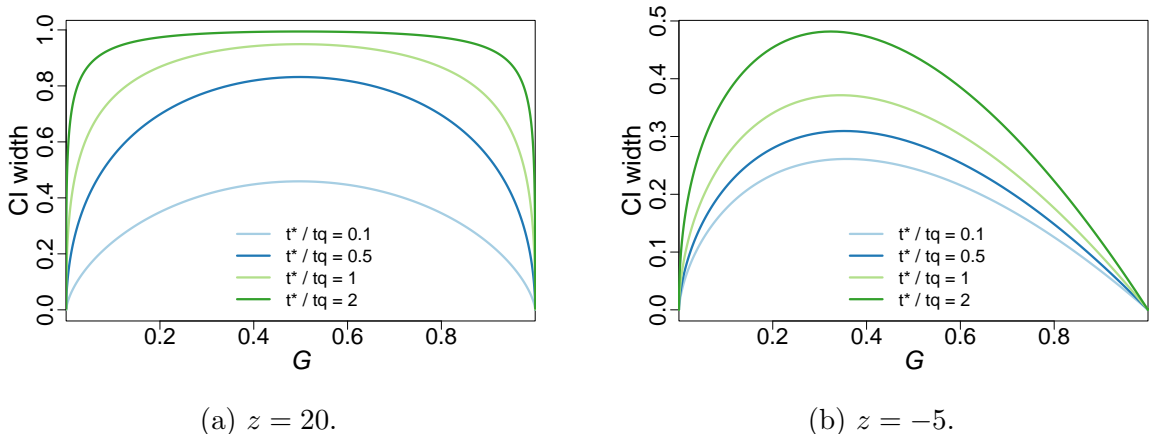


Figure 5: CI width as a function of G for four values of $t^*/t_q \in \{0.1, 0.5, 1, 2\}$ (with $q = 63$), computed by the w - z method. Panels show representative cases for (a) $z = 20$ (positive- z regime) and (b) $z = -5$ (negative- z regime).

When interpreting CI width, it is important to recognize that the (w, z) parameter space does not generate extinction probabilities uniformly across the full range of G . In fact, the vast majority of the (w, z) plane corresponds to regions where extinction is either extremely unlikely ($G \approx 0$) or almost certain ($G \approx 1$), while the zone of high uncertainty is confined to a narrow band near $w = 0$ when $z > 0$ (Fig. 6).

Accordingly, although CI-width or variance curves plotted against G may suggest poor estimability across much of the range in the $z > 0$ regime, this impression is misleading. As noted above, the intervals remain extremely tight near the boundaries ($G = 0, 1$), ensuring informative assessments in these regions. Reliable estimation therefore depends on where the system actually resides in (w, z) space: in most realistic cases the estimates of (w, z) are unlikely to fall exactly in the maximally uncertain region around $w = 0$, and more often lie in regions where extinction risk can be judged with confidence.

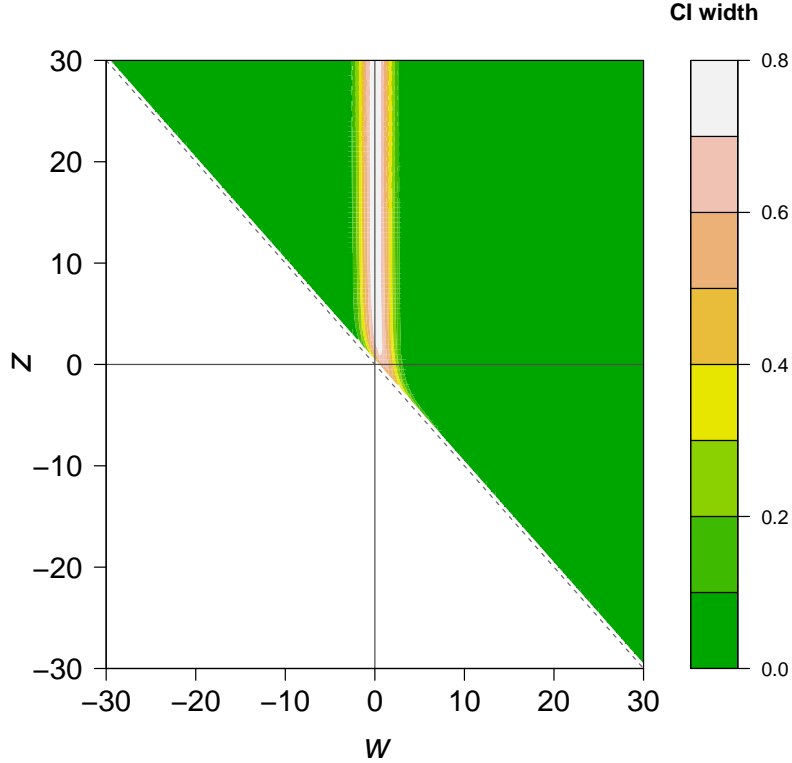


Figure 6: CI width for extinction risk estimation over the (w, z) parameter space. The contour plot shows how the CI width varies as a function of w and z , highlighting regions where the estimation uncertainty is highest (near $w = 0$, i.e., $G \approx 0.5$) and lowest (near $G = 0$ and $G = 1$). Here, $q = t_q = 63$ and $t^* = 25$. The CI width was calculated using the w - z method.

4.7.2 Effect-size perspective

It is useful to consider the reliability of extinction-risk estimation from the viewpoint of effect size. Following the effect-size literature (e.g., Cohen, 1988), an effect size indexes the magnitude of the phenomenon as determined by the model parameters; all else equal, larger effects are easier to detect and hence yield tighter CIs. Although one might be tempted to take the extinction probability itself as an effect size, the CI width is typically unimodal in G and is small near 0 and 1; therefore G alone is not a monotone index of inferential difficulty. A more informative index is the distance to the point(s) of maximal uncertainty:

$$G_{\max} := \arg \max_{G \in (0,1)} \text{Var}(\widehat{G}), \quad \Delta(G) := |G - G_{\max}|.$$

This distance increases as extinction becomes nearly certain or nearly impossible, and decreases in the ambiguous middle. In the central $z > 0$ regime, numerical computa-

tions indicate $G_{\max} \simeq 0.5$ (attained at $w = 0$). With this choice, estimation precision depends not only on the data (q, t_q) but also on the effect size $\Delta(G)$ and the underlying parameters (w, z, t^*) : for fixed data, larger $\Delta(G)$ yields narrower CIs, while the width is largest near G_{\max} . Equal values of G (or $\Delta(G)$) can nevertheless arise from different (w, z) configurations, which differ in sensitivity and in the sampling correlation $\rho(w, z, k)$, so that the effect-size index $\Delta(G)$ captures the main pattern but does not fully determine CI width.

4.7.3 Dependence on data

Dependence on the data enters in complementary ways. With t_q fixed, increasing the number of increments q improves precision primarily by stabilizing the variance estimator $\hat{\sigma}^2$ (Eq. (10)), yielding an initial $\sim q^{-1/2}$ reduction in CI width; however, the gain quickly saturates because $\text{Var}(\hat{\mu})$ is governed by t_q (not by q) and the noncentral- t law approaches its normal limit as the degrees of freedom grow. Beyond this point, additional increments no longer shrink the interval, which levels off at a value set by the ratio t^*/t_q (i.e., of order $\sqrt{t^*/t_q}$).

By contrast, lengthening the observation span t_q directly reduces $\text{Var}(\hat{\mu})$ (proportional to $1/t_q$) and increases t_q/t^* , both of which narrow the CI and yield a smaller asymptotic plateau. Consequently, for fixed t_q further increases in q cannot push the width below this plateau, whereas increasing t_q continues to deliver substantial gains.

Further analytic details, including asymptotics in the regimes $z > 0$ and $z \ll 0$, are developed in Appendix S7.

4.7.4 Dependence on the original parameters μ and σ^2

On the (w, z) plane (Fig. 6), the sign of μ is split by $w = z$. For $\mu > 0$, CIs are small almost everywhere; the uncertainty ridge lies near $w \approx 0$ (for fixed $\mu > 0$ and $x_d > 0$ the line $w = 0$ itself is not reached). For $\mu < 0$, the CI is maximized at $w = 0$ (that is, $-\mu t^* = x_d$) and is small elsewhere. With (μ, x_d, t^*) fixed, increasing σ moves (w, z) toward the origin along a fixed ray, widening the CI up to a data-limited plateau of order $\sqrt{t^*/t_q}$. Decreasing σ pushes (w, z) outward and the CI collapses rapidly at rate $\exp(-\text{const}/\sigma^2)$, except along the $w = 0$ ray (reachable only if $\mu = -x_d/t^*$). See Appendix S7.

4.7.5 Dependence on time horizon

As the time horizon t^* increases, the system moves along the (w, z) -plane trajectories in Fig. 7. When the growth rate is negative ($\mu < 0$), extinction risk shows a characteristic pattern. Even if near-term extinction is highly unlikely, extending the horizon eventually brings the trajectory to the line $w = 0$, which corresponds to the zone of maximal uncertainty, at which point the CI widens substantially. Beyond this point, uncertainty decreases again as extinction becomes virtually certain at longer horizons. By contrast, when the growth rate is positive ($\mu > 0$), the trajectory does not cross

$w = 0$, extinction risk remains small across horizons, and the CIs remain uniformly tight. Numerical values are provided in Table S8.1.

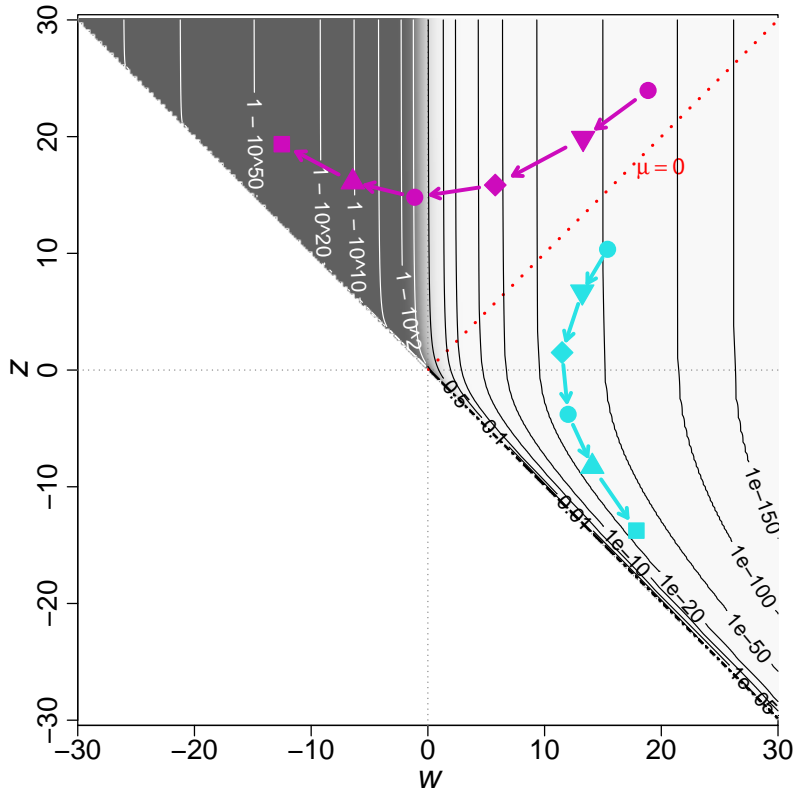


Figure 7: Time-horizon dependence of extinction risk. Varying the horizon t^* (with μ, σ, x_d fixed) shifts the system’s location in the (w, z) plane and thereby alters G . The curves trace (w, z) as t^* increases for two parameter sets: (a, magenta) $\mu < 0$ case (crosses $w = 0$; $\mu = -0.0589$, $\sigma = 0.1169$, $x_d = 12.64$); and (b, cyan) $\mu > 0$ case (does not cross $w = 0$; $\mu = 0.10$, $\sigma = 0.20$, $x_d = 13$). Symbols mark $t^* \in \{25.5, 42.5, 100, 250, 500, 1000\}$; arrows indicate increasing t^* .

4.8 Observation span required for precise estimation of extinction risk

The required data length depends strongly on the true extinction probability $G(w, z)$. When G is very small or very large, reliable inference is possible from much shorter series than might be expected, whereas uncertainty is greatest at intermediate values. To quantify this, I computed the minimal observation span t_q (unit-interval sampling, so $t_q = q$) needed for the upper bound of the 95% CI to lie below a management threshold $G_{\text{target}} = 0.1$. For each calculation z was fixed, w was adjusted to achieve the target G , and t_q was then solved numerically (details in Appendix S9).

Fig. 8 shows the required span relative to the horizon ($t^* = 100$ years). For both $z = -5$ and $z = 20$, only 10–20% of the horizon suffices when G is very small, while the requirement grows as G approaches intermediate values. The maximum occurs near $G = 0.5$ (outside the displayed range).

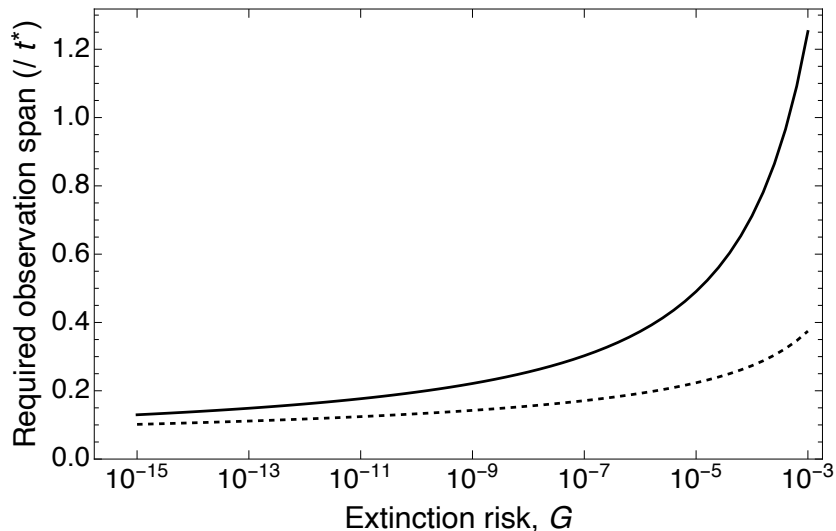


Figure 8: Required observation span for extinction-risk assessment. Shown is the minimal t_q/t^* , expressed as a fraction of the time horizon ($t^* = 100$ years), needed to ensure that the upper bound of the 95% CI for $G(w, z)$ lies below the management threshold $G_{\text{target}} = 0.1$. The solid line corresponds to $z = 20$, and the dashed line to $z = -5$. Even relatively short spans can be sufficient when the true risk is very small.

5 Extinction risk assessment of the Japanese eel

The Japanese eel (*Anguilla japonica*) was listed as Endangered on the IUCN Red List of Threatened Species in 2014. Its population has declined substantially, and eel aquaculture continues to depend heavily on the capture of juvenile glass eels from the wild. This reliance has raised concerns about recruitment and long-term productivity. The IUCN currently classifies the Japanese eel as Endangered under Criterion A, which is based solely on the magnitude of decline in abundance indices and geographic range. While such indicators highlight serious population loss, they do not directly quantify the probability of extinction. A more informative reassessment requires the application of Criterion E, which incorporates stochastic modeling to estimate future extinction risk. Using carefully compiled time-series data and a probabilistic framework, I estimate finite-horizon extinction probabilities under Criterion E to more accurately assess threat severity and inform conservation strategies.

To evaluate extinction risk under Criterion E, I analyzed three complementary time-series indices representing different life stages: glass eel catches from Shizuoka Prefecture, national elver catches in inland waters, and national yellow and silver eel catches

(Fig. 9). If a stable age distribution can be assumed (e.g., Caswell, 2001), interannual fluctuations should be similar among stages, so each series is informative for assessing overall extinction risk. This assessment adopts a precautionary approach: because the total population is much larger than the numbers represented in local catch records, the analysis was based on local data to obtain a conservative estimate of extinction risk, defined here as avoiding underestimation of the true risk. If extinction risk is low even for small local populations, the overall risk for the species should be even lower. Data sources, methodological details, and further justification are provided in Appendix S10, and the generation-time calculation with Criterion E thresholds is given in Appendix S11.

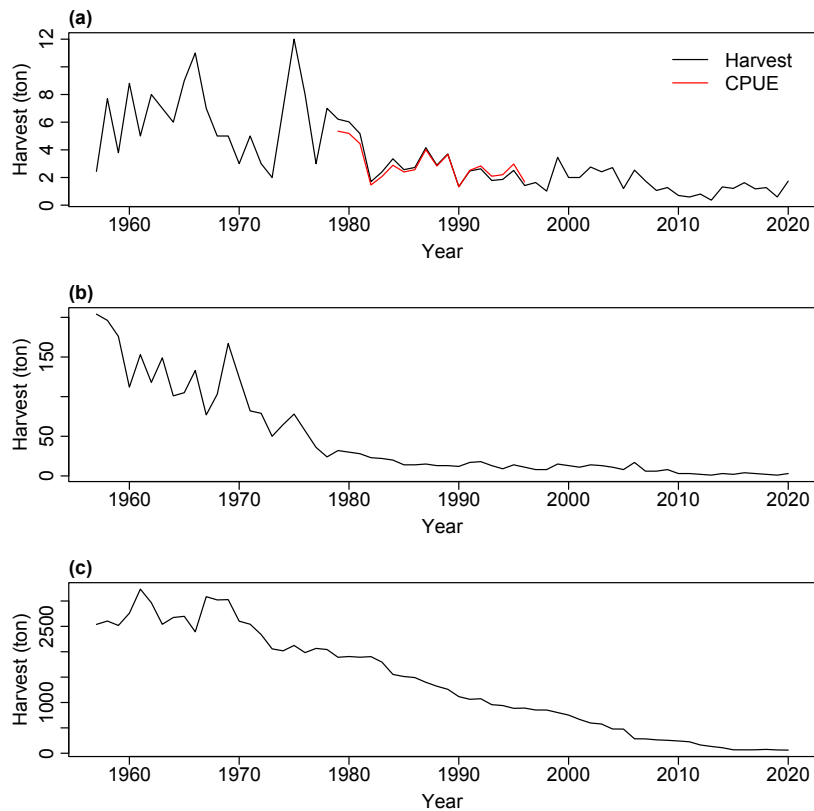


Figure 9: Time series of harvest and CPUE of Japanese eel (1957–2020). (a) Coastal glass eel in Shizuoka Prefecture: harvest for 1957–2020 and CPUE (catch per unit effort) for years with available effort data (1977–1997; red line). Catch closely tracks CPUE in the overlapping years, reflecting relatively stable fishing effort. (b) Inland seed fisheries (glass eels and elvers), national totals. (c) Inland eel fisheries (yellow and silver eels), national totals.

The extinction risk estimates for the Japanese eel, derived from fishery data and the statistical methods developed in this study, do not support classification as Critically Endangered (CR) or Endangered (EN) at any life stage (Table 1). For the CR and

EN time frames, the estimated probabilities were small and the CIs narrow, indicating confidence in a low probability of extinction by the corresponding time horizons. Although point estimates also fell below the Vulnerable (VU) threshold, some CIs were comparatively wide, leaving VU classification inconclusive and highlighting the need for additional data.

Table 1: Estimated extinction probabilities (point estimates and 95% CIs) for the Japanese eel.

Time-series	$\hat{\mu}$	$\hat{\sigma}^2$	\hat{x}_d	CR: $\hat{G}(t^* = 25.5)$	EN: $\hat{G}(t^* = 42.5)$	VU: $\hat{G}(t^* = 100)$
Glass eel	-0.0054 (-0.15, 0.14)	0.33 (0.24, 0.49)	16.0	5×10^{-8} (4×10^{-12} , 1×10^{-4})	3×10^{-5} (5×10^{-9} , 0.012)	0.007 (7×10^{-7} , 0.51)
Glass and elver eel	-0.07 (-0.17, 0.04)	0.17 (0.12, 0.26)	12.4	3×10^{-7} (5×10^{-11} , 3×10^{-4})	3×10^{-4} (2×10^{-7} , 0.05)	0.11 (1×10^{-4} , 0.90)
Yellow and silver eel	-0.059 (-0.089, -0.029)	0.014 (0.010, 0.020)	12.6	2×10^{-79} (2×10^{-109} , 3×10^{-52})	2×10^{-40} (1×10^{-57} , 3×10^{-25})	5×10^{-9} (5×10^{-17} , 1×10^{-3})

Note. Each cell reports the ML point estimate with the 95% CI in parentheses. Extinction probability is evaluated as $\hat{G}(t^*) = \Pr[T \leq t^*]$, with $t^* \in \{25.5, 42.5, 100\}$ years corresponding to CR, EN, and VU horizons, respectively.

6 Discussion

The central implication of these results is that reliable extinction-risk inference is often achievable even with relatively short time series. Although intermediate extinction risks can produce zones of high uncertainty, the analysis shows that such cases are confined to specific regions of parameter space and are not the general rule. This perspective helps to reconcile earlier debates: prior simulation and empirical studies had reported accurate forecasts with moderate data lengths (Holmes *et al.*, 2007; Brook *et al.*, 2000), despite concerns about long-term precision (Fieberg & Ellner, 2000; Ellner & Holmes, 2008). The present framework explains when and why these results arise and clarifies the limits of inferences based on previous CI-construction methods.

Practically, population viability analysis should not be dismissed solely due to short records. When extinction probability is far from intermediate values, even modest observation spans can provide informative intervals; Criterion E assessments can therefore be applied more broadly to support conservation decisions. The required-span analysis (Section 4.8) shows that confirming $G(t^*) \leq G_{\text{thr}}$ may demand only a fraction of the forecasting horizon when true risk is small (Fig. 8).

From a design standpoint, replication q and span t_q play complementary roles (Section 4.7). Increasing q initially narrows CIs, but the gain soon saturates as the noncentral- t laws approach normality. In contrast, lengthening t_q continues to reduce

interval width by lowering the plateau set by t^*/t_q . This is actionable for monitoring design: once q is moderate, extending span is often more valuable than densifying sampling.

Time-horizon dependence also admits a transparent interpretation (Section 4.7). Contrary to the notion that forecasts inevitably lose reliability at longer horizons, the model shows that uncertainty peaks at intermediate horizons near the $w = 0$ crossing. For $\mu < 0$, extinction is unlikely in the near term but becomes virtually certain as t^* grows, producing the observed non-monotonic pattern in CI width. This behavior reflects the biological reality that extinction is ultimately inevitable on long time scales. For $\mu > 0$, trajectories do not cross $w = 0$, so the model yields uniformly narrow CIs; however, because density dependence is not included, the model does not capture eventual extinction in this case.

Applied to the Japanese eel time series, the estimated extinction probabilities over 25.5, 42.5, and 100 years lie well below the thresholds for Critically Endangered or Endangered under Criterion E, with narrow intervals across the three series (Table 1). These findings reveal a clear discrepancy from Criterion A, which is based on observed rates of decline and does not incorporate absolute population size or stochastic persistence. When Mace & Lande (1991) proposed a precursor to the IUCN Red List framework, the assumed population sizes were evidently small: they explicitly listed effective population sizes N_e , with $N_e < 50$ for Critically Endangered (CR), $N_e < 500$ for Endangered (EN), and $N_e < 2000$ for Vulnerable (VU). The framework was likely designed to align the outcomes of Criterion E PVAs with those of Criterion A assessments based solely on rates of decline. Contrary to the original intention, the current IUCN Criterion A is also applied to large populations, including many fish stocks, leading to systematic overestimation of extinction risk.

Several assumptions and limitations merit emphasis. The diffusion model assumes lognormal increments with constant drift and variance, no density dependence, and error-free observation of abundance indices. Autocorrelated environmental variation, demographic stochasticity, and observation error can violate these assumptions, affecting $(\hat{\mu}, \hat{\sigma}^2)$ and hence (\hat{w}, \hat{z}) and the resulting CIs. Statistically, unmodeled variation tends to be absorbed into $\hat{\sigma}^2$, as the model attributes unexplained changes to environmental stochasticity; this can overstate extinction risk when other sources of uncertainty are present but not explicitly modeled, although the net effect is context-specific. The CI construction relies on independence of the drift and variance estimators (yielding noncentral- t sampling laws), which holds under the Gaussian model but would require revision for heavy-tailed or state-dependent noise. Despite these limitations, simple models often perform well on complex systems (e.g., Iwasa *et al.*, 1987; Lande & Orzack, 1988; Hakoyama & Iwasa, 2005), and the present results suggest that reliable inference remains possible under modest departures from assumptions. Additional complications such as intermittent changes in fishing effort, structural breaks, and reporting gaps or aggregation artifacts in catch-based indices may further distort inference. To mitigate these issues, I selected time series with better continuity and interpreted coastal and inland data separately (Appendix S10), though some residual bias may persist.

7 Conclusion

The w - z framework recasts the question of data sufficiency as a geometric and statistical problem with tractable solutions, delivering CIs with dependable coverage. Accordingly, when extinction risk is far from intermediate values, reliable probability estimates can be obtained from relatively short time series.

Critiques of PVA often emphasize its imprecision with limited data and recommend proxy-based alternatives. Yet such proxies provide neither explicit extinction probabilities nor a principled way to assess reliability. As Brook *et al.* (2002) argued, there is little reason to abandon PVA in favor of less transparent alternatives. Even when uncertainty is substantial, PVA remains the only framework that directly quantifies extinction risk and reports the precision of its own forecasts.

For species with large populations, such as the Japanese eel, extinction risk is often low enough that meaningful quantitative assessment can be achieved even with limited data. In the present case, the results indicate that, under Criterion E of the IUCN Red List, the Japanese eel does not meet the EN or CR thresholds. Consequently, conservation resources for Endangered or Critically Endangered species should not be diverted to avert extinction of this species, but rather allocated to taxa that are truly at risk. Nonetheless, the risk of fishery decline remains substantial and could lead to serious ecological and socioeconomic consequences. Accordingly, management of the Japanese eel should focus on the long-term sustainability of food production rather than on extinction avoidance per se. This principle also applies to other harvested species with large populations.

References

- Blanchard, P., Higham, D.J. & Higham, N.J. (2021) Accurately computing the log-sum-exp and softmax functions. *IMA Journal of Numerical Analysis*, **41**, 2311–2330. <https://dx.doi.org/10.1093/imanum/draa038>.
- Brook, B.W., Burgman, M.A., Akcakaya, H.R., O’Grady, J.J. & Frankham, R. (2002) Critiques of PVA ask the wrong questions: Throwing the heuristic baby out with the numerical bath water. *Conservation Biology*, **16**, 262–263. <https://dx.doi.org/10.1046/j.1523-1739.2002.01426.x>.
- Brook, B.W., O’Grady, J.J., Chapman, A.P., Burgman, M.A., Akcakaya, H.R. & Frankham, R. (2000) Predictive accuracy of population viability analysis in conservation biology. *Nature*, **404**, 385–387. <https://dx.doi.org/10.1038/35006050>.
- Caswell, H. (2001) *Matrix population models*. Sinauer Associates, Sunderland, MA.
- Coale, A.J. (1972) *Growth and Structure of Human Populations: A Mathematical Investigation*. Princeton University Press, Princeton.

- Cohen, J. (1988) *Statistical power analysis for the behavioral sciences*. Lawrence Erlbaum Associates, New York.
- Cox, D.R. & Miller, H.D. (1965) *The theory of stochastic processes*. Chapman and Hall, London.
- Dennis, B., Munholland, P.L. & Scott, J.M. (1991) Estimation of growth and extinction parameters for endangered species. *Ecological Monographs*, **61**, 115–143. <https://dx.doi.org/10.2307/1943004>.
- Efron, B. & Tibshirani, R.J. (1993) *An introduction to the bootstrap*. Chapman and Hall, London.
- Ellner, S.P. (2003) When does parameter drift decrease the uncertainty in extinction risk estimates? *Ecology Letters*, **6**, 1039–1045. <https://dx.doi.org/10.1046/j.1461-0248.2003.00538.x>.
- Ellner, S.P., Fieberg, J., Ludwig, D. & Wilcox, C. (2002) Precision of population viability analysis. *Conservation Biology*, **16**, 258–261. <https://dx.doi.org/10.1046/j.1523-1739.2002.00553.x>.
- Ellner, S.P. & Holmes, E.E. (2008) Commentary on Holmes et al.(2007): resolving the debate on when extinction risk is predictable. *Ecology Letters*, **11**, E1–E5. <https://dx.doi.org/10.1111/j.1461-0248.2008.01211.x>.
- Fieberg, J. & Ellner, S.P. (2000) When is it meaningful to estimate an extinction probability? *Ecology*, **81**, 2040–2047. [https://dx.doi.org/10.1890/0012-9658\(2000\)081\[2040:WIIMTE\]2.0.CO;2](https://dx.doi.org/10.1890/0012-9658(2000)081[2040:WIIMTE]2.0.CO;2).
- Geary, R. (1936) The distribution of “student’s” ratio for non-normal samples. *Supplement to the Journal of the Royal Statistical Society*, **3**, 178–184. <https://dx.doi.org/10.2307/2983669>.
- Giner, G. & Smyth, G.K. (2016) statmod: probability calculations for the inverse Gaussian distribution. *arXiv preprint arXiv:160306687*. <https://dx.doi.org/10.48550/arXiv.1603.06687>.
- Gordon, R.D. (1941) Values of Mills’ ratio of area to bounding ordinate and of the normal probability integral for large values of the argument. *The Annals of Mathematical Statistics*, **12**, 364–366. <https://dx.doi.org/10.1214/aoms/1177731721>.
- Hakoyama, H. & Iwasa, Y. (2000) Extinction risk of a density-dependent population estimated from a time series of population size. *Journal of Theoretical Biology*, **204**, 337–359. <https://dx.doi.org/10.1006/jtbi.2000.2019>.

- Hakoyama, H., Fujimori, H., Okamoto, C. & Kodama, S. (2016) Compilation of Japanese fisheries statistics for the Japanese eel, *Anguilla japonica*, since 1894: a historical dataset for stock assessment. *Ecological Research*, **31**, 153–153. <https://dx.doi.org/10.1007/s11284-015-1332-9>.
- Hakoyama, H. & Iwasa, Y. (2005) Extinction risk of a meta-population: aggregation approach. *Journal of Theoretical Biology*, **232**, 203–216. <https://dx.doi.org/10.1016/j.jtbi.2004.08.008>.
- Halley, J.M. (2003) Parameter drift stabilizes long-range extinction forecasts. *Ecology Letters*, **6**, 392–397. <https://dx.doi.org/10.1046/j.1461-0248.2003.00452.x>.
- Han, Y.S., Tzeng, W.N. & Liao, I.C. (2009) Time series analysis of Taiwanese catch data of Japanese glass eels *Anguilla japonica*: possible effects of the reproductive cycle and El Niño events. *Zoological Studies*, **48**, 632–639.
- Holmes, E.E., Sabo, J.L., Viscido, S.V. & Fagan, W.F. (2007) A statistical approach to quasi-extinction forecasting. *Ecology Letters*, **10**, 1182–1198. <https://dx.doi.org/10.1111/j.1461-0248.2007.01105.x>.
- IUCN (2012) *IUCN Red List Categories and Criteria: Version 3.1*. IUCN, Gland, Switzerland and Cambridge, UK, second edition.
- Iwasa, Y., Andreasen, V. & Levin, S. (1987) Aggregation in model ecosystems. I. Perfect aggregation. *Ecological Modelling*, **37**, 287–302. [https://dx.doi.org/10.1016/0304-3800\(87\)90030-5](https://dx.doi.org/10.1016/0304-3800(87)90030-5).
- Kotake, A., Okamura, A., Yamada, Y., Utoh, T., Arai, T., Miller, M.J., Oka, H.P. & Tsukamoto, K. (2005) Seasonal variation in the migratory history of the Japanese eel *Anguilla japonica* in Mikawa Bay, Japan. *Marine Ecology Progress Series*, **293**, 213–221.
- Kotake, A., Arai, T., Okamura, A., Yamada, Y., Utoh, T., Oka, H.P., Miller, M.J. & Tsukamoto, K. (2007) Ecological aspects of the Japanese eel, *Anguilla japonica*, collected from coastal areas of Japan. *Zoological Science*, **24**, 1213–1221. <https://dx.doi.org/10.2108/zsj.24.1213>.
- Lande, R. & Orzack, S.H. (1988) Extinction dynamics of age-structured populations in a fluctuating environment. *Proceedings of the National Academy of Sciences of the United States of America*, **85**, 7418–7421. <https://dx.doi.org/10.1073/pnas.85.19.7418>.
- Ludwig, D. (1999) Is it meaningful to estimate a probability of extinction? *Ecology*, **80**, 298–310. [https://dx.doi.org/10.1890/0012-9658\(1999\)080\[0298:IIMTEA\]2.0.CO;2](https://dx.doi.org/10.1890/0012-9658(1999)080[0298:IIMTEA]2.0.CO;2).

- Mace, G.M. & Lande, R. (1991) Assessing extinction threats: toward a reevaluation of IUCN threatened species categories. *Conservation Biology*, **5**, 148–157. <https://dx.doi.org/10.1111/j.1523-1739.1991.tb00119.x>.
- Vøllestad, L.A. (1992) Geographic variation in age and length at metamorphosis of maturing European eel: environmental effects and phenotypic plasticity. *Journal of Animal Ecology*, **61**, 41–48. <https://dx.doi.org/10.2307/5507>.
- Yokouchi, K., Sudo, R., Kaifu, K., Aoyama, J. & Tsukamoto, K. (2009) Biological characteristics of silver-phase Japanese eels, *Anguilla japonica*, collected from Hamana Lake, Japan. *Coastal Marine Science*, **33**, 54–63.

Author contributions

Hiroshi Hakoyama conceived and designed the study, conducted the analyses, and wrote the manuscript.

Acknowledgements

This research was funded by a grant from the Japan Fisheries Agency.

Conflict of interest statement

The author declares no conflicts of interest.

Data availability statement

All data used in this study are from publicly available sources.

Nationwide eel fisheries statistics are primarily from Hakoyama *et al.* (2016), which compiles annual Japanese fisheries statistics since 1894. To extend coverage, I also used the *Annual Reports of Catch Statistics on Fishery and Aquaculture in Japan* for recent years, including inland yellow and silver eel harvests.

For Shizuoka Prefecture, coastal glass eel harvests were compiled from the *Annual Reports of Catch Statistics on Fishery and Aquaculture* (1957–1978), the *Annual Reports of the Shizuoka Prefectural Fisheries Experiment Station* (1979–2004; ISSN 2759-2340), and the public bulletin *Hamana* (2005–2020; https://fish-exp.pref.shizuoka.jp/hamanako/6_pro/hamana_backnumber.html).

Glass eel catch and fisher-number data from the *Eel Culture Research Council* annual reports (Volumes 7–27, 1977–1997) were used to compute CPUE for Shizuoka Prefecture; library holdings are listed in CiNii (NCID: AN10187528).

Supporting information

Appendix S1. Numerical Stability of $G(w, z)$

This appendix studies numerically stable evaluation of

$$G(w, z) = \Phi(-w) + \exp\left(\frac{z^2 - w^2}{2}\right) \Phi(-z) \quad \text{for } w + z > 0, \quad w, z \in \mathbb{R}, \quad (\text{S1.1a})$$

$$Q(w, z) = 1 - G(w, z), \quad (\text{S1.1b})$$

for real w and z satisfying $w + z > 0$. Here, $\Phi(x)$ denotes the standard normal cumulative distribution function. The two functions are complementary by definition.

The key numerical challenges in evaluating (S1.1) in double-precision arithmetic are:

- (i) Overflow: for large z , the exponential $\exp((z^2 - w^2)/2)$ can overflow. Overflow occurs whenever $(z^2 - w^2)/2 > \log(\text{DBL_MAX})$; in the worst case $w = 0$ this corresponds to $z \gtrsim 37.7$.
- (ii) Loss of Information (LOI): The summands of (S1.1) can be highly unbalanced, causing smaller terms to be rounded to zero. This is particularly problematic in the region $w \ll 0$, where the extinction probability G is very close to 1 but is rounded to unity in double precision.
- (iii) Probabilities beyond double-precision limits: when G or Q falls below the minimum positive number representable in double precision ($\text{DBL_TRUE_MIN} \approx 4.94 \times 10^{-324}$) the linear-scale arithmetic path underflows to 0.

Accurate evaluation in cases (ii) and (iii) is particularly important because extinction probabilities inferred from data can be extremely small or extremely large, so values of G near 0 or 1 naturally arise. Although probabilities such as 10^{-9} and 10^{-20} may both appear negligible, they lead to markedly different confidence interval widths and therefore must be resolved with numerical accuracy.

I adopt three complementary strategies to address these issues. First, the use of a Mills ratio representation for large z (next subsection) replaces the numerically unstable product $\exp((z^2 - w^2)/2) \Phi(-z)$ with a product of moderate-magnitude factors. Second, for large negative w , the complementary probability $Q(w, z) = 1 - G(w, z)$ is evaluated instead of $G(w, z)$ itself, thereby avoiding loss of information near unity. Third, I evaluate sums and differences on the log scale using stable identities (log-sum-exp and log-difference), which preserve information even when G lies outside the representable range $4.94 \times 10^{-324} < G < 1 - 4.94 \times 10^{-324}$.

S1.1 Linear-scale formulation, Mills switch, and validation

The asymptotic expansion of the Mills ratio and the identity used below are standard facts and are also employed in the appendix of Dennis *et al.* (1991).

Let $\phi(x) = \Phi'(x) = \frac{1}{\sqrt{2\pi}} \exp(-x^2/2)$ denote the standard normal density. The Mills ratio, defined for positive arguments $z > 0$, is

$$R(z) = \frac{\Phi(-z)}{\phi(z)}.$$

As $z \rightarrow \infty$, it admits the asymptotic expansion

$$R(z) \sim \sum_{k=0}^{\infty} \frac{(-1)^k (2k-1)!!}{z^{2k+1}}. \quad (\text{S1.2})$$

The eight-term truncation $S_7(z)$ of (S1.2) (i.e., $k = 0, \dots, 7$)

$$S_7(z) := \frac{1}{z} - \frac{1}{z^3} + \frac{3}{z^5} - \frac{15}{z^7} + \frac{105}{z^9} - \frac{945}{z^{11}} + \frac{10395}{z^{13}} - \frac{135135}{z^{15}}$$

is used in the numerical implementation whenever $z \geq z_{\text{thr}}$.

The identity relating the two terms is

$$\exp\left(\frac{z^2 - w^2}{2}\right) \Phi(-z) = \phi(w) R(z). \quad (\text{S1.3})$$

This motivates the switched linear-scale definitions

$$G_{\text{lin}}(w, z; z_{\text{thr}}) = \begin{cases} \Phi(-w) + \exp((z^2 - w^2)/2) \Phi(-z), & z < z_{\text{thr}}, \\ \Phi(-w) + \phi(w) S_7(z), & z \geq z_{\text{thr}}, \end{cases} \quad (\text{S1.4})$$

$$Q_{\text{lin}}(w, z; z_{\text{thr}}) = \begin{cases} \Phi(w) - \exp((z^2 - w^2)/2) \Phi(-z), & z < z_{\text{thr}}, \\ \Phi(w) - \phi(w) S_7(z), & z \geq z_{\text{thr}}. \end{cases}$$

G_{lin} and Q_{lin} denote the double-precision linear-scale implementations, which switch to the Mills ratio expansion beyond the threshold z_{thr} . The Mills ratio representation never overflows and, for large z , provides higher accuracy by avoiding the cancellation between the exponential and $\Phi(-z)$ in (S1.1a).

Numerical accuracy validation on the linear scale. Numerical accuracy of the double-precision implementations is assessed by comparison with high-precision references computed with MPFR. In the double-precision path, Φ and ϕ are evaluated via R's `pnorm()` and `dnorm()`. High-precision references are computed with `Rmpfr` by calling the same functions on `mpfr` arguments, with the precision explicitly set to `precBits = 128`. The references are always based on the exact analytic forms (S1.1a)–(S1.1b), whereas the double-precision path may employ approximations such as the Mills expansion (S1.4); discrepancies therefore reflect both numerical precision and the chosen approximation. To reduce cancellation, the expression $(z^2 - w^2)/2$ is evaluated in factored form $(z + w)(z - w)/2$ in numerical implementations. All arithmetic operations

for the references, including the summation of terms such as $\Phi(-w) + \phi(w)R(z)$ and the evaluation of logarithms, are carried out entirely in MPFR so that no rounding to double occurs during intermediate steps. The result is converted back to double precision only after these operations are completed, for comparison with the double-precision approximations. Validation then compares the high-precision MPFR references with double-precision results on a regular grid, defined by $w \in [w_{\min}, w_{\max}]$ and $z \in [z_{\min}, z_{\max}]$, subject to the strict mask $w + z > 0$ (Fig. S1.1).

Errors are evaluated with a log-scale metric based on $\log G_{\text{lin}}$ and the MPFR reference $\log G_{\text{ref}}$, applied consistently to both the linear-scale implementations and the log-scale formulation described in the next subsection.

For each grid point the relative error is recorded as

$$\varepsilon_{\text{lin}} = |\exp(\log G_{\text{lin}} - \log G_{\text{ref}}) - 1|, \quad d_{\text{lin}} = -\log_{10}(\max(\varepsilon_{\text{lin}}, 10^{-16})). \quad (\text{S1.5})$$

Here ε_{lin} coincides with the conventional relative error $|G_{\text{lin}} - G_{\text{ref}}|/G_{\text{ref}}$ whenever both values are positive and well resolved. The same definitions are applied to Q in place of G . Digits of accuracy d_{lin} are capped at 16 to avoid divergence in the case of exact matches. In the implementation, the function $\exp(x) - 1$ is evaluated using the numerically stable routine `expm1` in R.

Because relative error is ill-posed where the double-precision representation of the reference would round to 0 or 1, two loss-of-information (LOI) flags are introduced based on the reference logs, where “ref” denotes either G_{ref} or Q_{ref} :

$$\text{LOI}_1 : \log(1 - \text{ref}) < \log \tau_1, \quad \text{LOI}_0 : \log(\text{ref}) < \log \tau_0,$$

with thresholds $\tau_1 = 10^{-15}$ and $\tau_0 = 10^{-308}$. Points flagged as LOI are excluded from accuracy evaluation.

A scan over z_{thr} (Fig. S1.2) maximizes the joint mean digits $\min\{\text{mean}_G, \text{mean}_Q\}$ and exhibits a broad plateau with values above 13 digits, with an optimum near $z_{\text{thr}} \approx 18.7$.

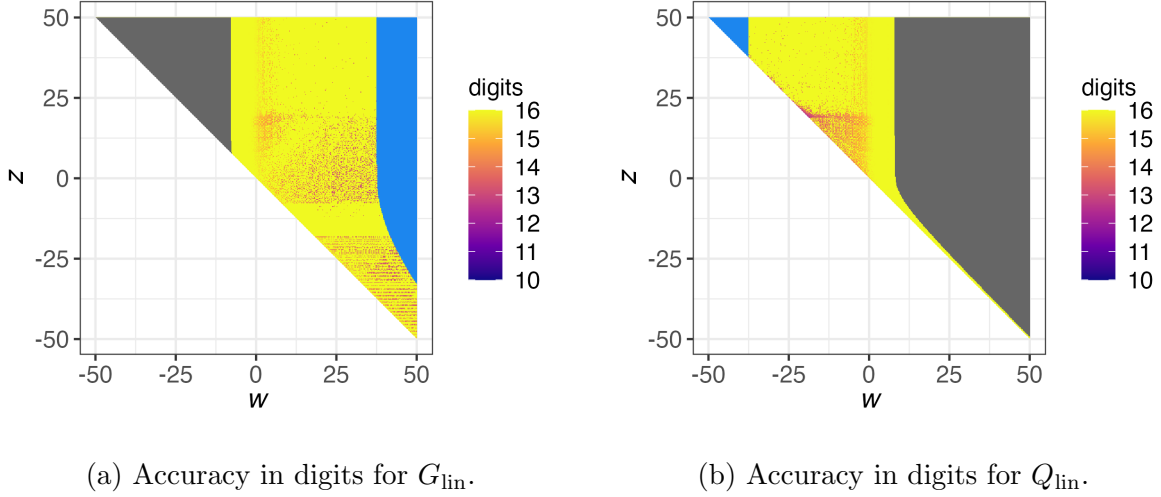


Figure S1.1: Accuracy of G_{lin} and Q_{lin} on a regular grid. Heatmap colors encode digits of accuracy with $z_{\text{thr}} = 19$. Regions of loss of information ($\text{LOI}_1/\text{LOI}_0$) are excluded from the statistics (gray: LOI_1 , light blue: LOI_0).

As shown in Fig. S1.1a–b, in the region $w \ll 0$, $G_{\text{lin}} \approx 1$ and its linear evaluation is ill-conditioned. This is because the second term in G_{lin} is extremely small, while the first term is nearly one. On the other hand, Q_{lin} remains representable because both terms are small but their difference avoids the same loss of precision. Therefore, in the $w \ll 0$ region I evaluate Q_{lin} and return the extinction probability G in the form $1 - Q_{\text{lin}}$. This notation indicates that Q_{lin} is computed directly and then used symbolically in $1 - Q_{\text{lin}}$, rather than numerically recombining two floating-point numbers close to 1. Symmetrically, for $w \gg 0$ I evaluate G_{lin} and (if necessary) return Q as $1 - G_{\text{lin}}$.

For clarity, define the linear-scale hybrid return value

$$G_{\text{lin,hyb}}(w, z) := \begin{cases} G_{\text{lin}}(w, z; z_{\text{thr}}), & w \geq 0, \\ 1 - Q_{\text{lin}}(w, z; z_{\text{thr}}), & w < 0. \end{cases}$$

This complementary w switching is independent of and applied simultaneously with the z Mills switch, thereby extending the reliable evaluation region to most of the (w, z) domain. The only exception is the LOI_0 region, where values of G fall outside the representable range of double precision. Since the smallest positive double is $2^{-1074} \approx 4.94 \times 10^{-324}$, the admissible domain is bounded by

$$4.94 \times 10^{-324} < G_{\text{lin,hyb}} < 1 - 4.94 \times 10^{-324}.$$

The remaining challenge is estimation in the LOI_0 region, which will be addressed in the next section by logarithmic evaluation.

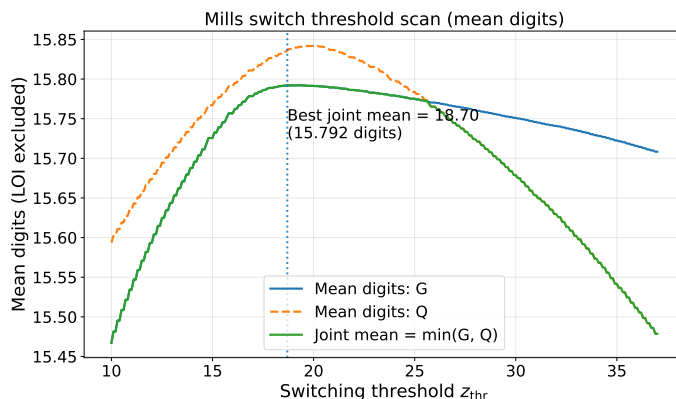


Figure S1.2: Mean digits of accuracy (log scale metric, LOI excluded) versus the z -direction Mills switch threshold z_{thr} ; the vertical dashed line indicates the threshold that maximizes the joint mean $\min\{\text{mean}_G, \text{mean}_Q\}$. For the grid and precision used here the optimum occurs near $z_{\text{thr}} \approx 18.7$.

Range extension on the log scale. Working on the log scale removes the hard double-precision bound $G > 4.94 \times 10^{-324}$ imposed on the linear representation. Because the most negative finite double that can be represented is $-\text{DBL_MAX} \approx -1.80 \times 10^{308}$, the admissible window expands from this linear-scale interval to

$$\exp(-1.80 \times 10^{308}) < G_{\log} < 1 - \exp(-1.80 \times 10^{308}), \quad (\text{S1.6})$$

where the endpoint $\exp(-\text{DBL_MAX})$ is kept *symbolically*, because its direct evaluation in double precision would underflow to 0. This widens the range by more than 7.8×10^{307} orders of magnitude (base-10), i.e., $\Delta \log_{10} \approx 7.8 \times 10^{307}$.

All subsequent operations are carried out in the log scale, so values as small as $\log G \approx -1.80 \times 10^{308}$ remain representable. Although converting such extremes back to linear scale inevitably rounds to 0, the probabilities themselves can still be *reported* in scientific form $a \times 10^b$ by formatting $\log_{10} G$ instead of evaluating G . Consequently, every (w, z) pair encountered in population-viability applications is evaluable without underflow, and the $\text{LOI}_{\text{LOG}0}$ region lies far outside the biologically relevant domain.

S1.2 Log-scale formulation and stable transforms

The log scale is introduced to address challenge (iii), namely probabilities beyond the limits of double precision. When G or Q falls below the minimum positive number representable in double precision ($\text{DBL_TRUE_MIN} \approx 4.94 \times 10^{-324}$), linear-scale arithmetic underflows to zero, and no departure from zero can be resolved. If numbers smaller than this bound were representable, then in combination with the complementary evaluation described in the previous subsection, it would be possible to evaluate extinction probabilities closer to one than $1 - 4.94 \times 10^{-324}$. To preserve information in such tails, I evaluate G (and similarly Q) on the log scale, where sums and differences

of exponentials are computed using stable identities such as the log-sum-exp and log-difference forms. These transforms have been analyzed for rounding error, for example by Blanchard *et al.* (2021), and are stable under floating-point arithmetic.

Let $a = \log \Phi(-w)$ and $b = (z^2 - w^2)/2 + \log \Phi(-z)$, which are strictly negative throughout the admissible domain $w + z > 0$. Then

$$\log G(w, z) = \log \left(\Phi(-w) + \exp \left(\frac{z^2 - w^2}{2} \right) \Phi(-z) \right) = \log(e^a + e^b), \quad (\text{S1.7})$$

which is evaluated via the log-sum-exp identity

$$\log(e^a + e^b) = \max(a, b) + \log(1 + \exp(-|a - b|)). \quad (\text{S1.8})$$

By definition $Q(w, z) = 1 - G(w, z)$. With $c = \log \Phi(w)$, and since $Q(w, z) = \Phi(w) - e^b \geq 0$ for $w + z > 0$, it follows that $e^b \leq \Phi(w)$ and thus $c > b$. Accordingly, the log-difference identity can be applied directly, without case distinctions:

$$\log Q(w, z) = \log(e^c - e^b) = c + \log(1 - \exp(b - c)). \quad (\text{S1.9})$$

In practice, `log1p` is used in (S1.8), and `log1p/expm1` are used in (S1.9) when $b - c$ is near zero to avoid loss of significance.

Overflow cannot occur in the log scale. Nevertheless, for $z \gg 0$ the Mills ratio approximation $S_7(z)$ is accurate, and it is numerically convenient to retain in the log scale the same large- z branch as in the linear domain (Eq. (S1.4)). Reusing a and c from above, and introducing

$$\tilde{b} = \log \phi(w) + \log S_7(z),$$

one has $c > \tilde{b}$, so the log scale switching forms are

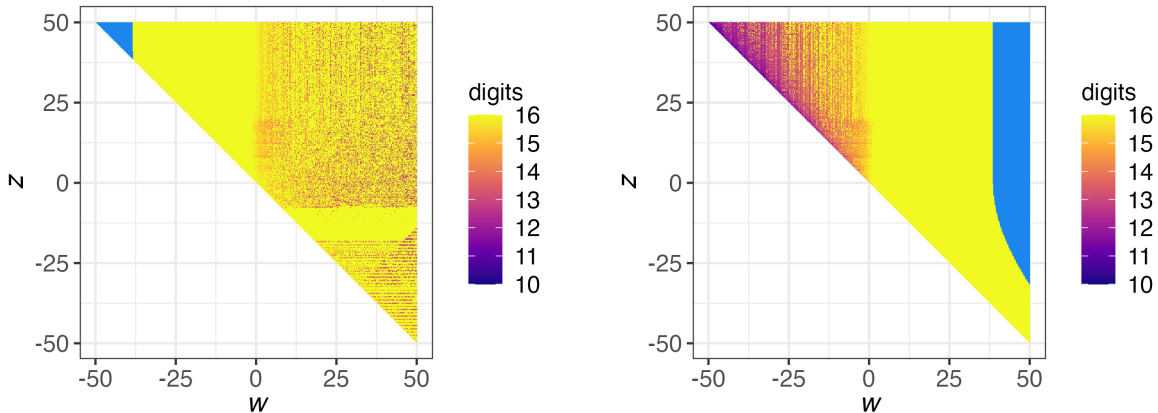
$$\begin{aligned} \log G_{\log}(w, z; z_{\text{thr}}) &= \begin{cases} \max(a, b) + \log(1 + \exp(-|a - b|)), & z < z_{\text{thr}}, \\ \max(a, \tilde{b}) + \log(1 + \exp(-|a - \tilde{b}|)), & z \geq z_{\text{thr}}, \end{cases} \\ \log Q_{\log}(w, z; z_{\text{thr}}) &= \begin{cases} c + \log(1 - \exp(b - c)), & z < z_{\text{thr}}, \\ c + \log(1 - \exp(\tilde{b} - c)), & z \geq z_{\text{thr}}. \end{cases} \end{aligned} \quad (\text{S1.10})$$

Numerical accuracy validation on the log scale. As in the linear scale, accuracy on the log scale is measured by the relative error computed from the log scale outputs,

$$\varepsilon_{\log} = |\exp(\log G_{\log} - \log G_{\text{ref}}) - 1|, \quad d_{\log} = -\log_{10}(\max(\varepsilon_{\log}, 10^{-16})). \quad (\text{S1.11})$$

Here $\log G_{\log}$ denotes the log scale evaluations defined in (S1.10), while $\log G_{\text{ref}}$ denotes high-precision MPFR reference values computed from the defining expression (S1.7) without the Mills approximation. The computation of references, the precision setting

(`precBits = 128`), the digits cap at 16, and the evaluation of $(z^2 - w^2)/2$ in factored form $(z + w)(z - w)/2$ are identical to the linear-scale validation. On the log scale, certain outputs carry no tail information and are flagged as LOI: $\log G = 0$ or $\log Q = 0$; $\log G = -\infty$ or $\log Q = -\infty$; and NaN, which is internally mapped to $-\infty$ and treated as the boundary case $G = 0$ or $Q = 0$. Validation then compares the high-precision MPFR references with double-precision log scale results on a regular grid, defined by $w \in [w_{\min}, w_{\max}]$ and $z \in [z_{\min}, z_{\max}]$, subject to the mask $w + z > 0$ (Fig. S1.3).



(a) Accuracy in digits for $\log G_{\log}$.

(b) Accuracy in digits for $\log Q_{\log}$.

Figure S1.3: Accuracy of $\log G_{\log}$ and $\log Q_{\log}$ on a regular grid. Heatmap colors encode digits of accuracy with $z_{\text{thr}} = 19$. Regions of loss of information ($\text{LOI}_{\text{LOG}0}$ and $\text{LOI}_{\text{LOG}\infty}$) are excluded from the statistics (light blue: $\text{LOI}_{\text{LOG}0}$, gray: $\text{LOI}_{\text{LOG}\infty}$).

As shown in Figs S1.3a and b, the two complementary evaluations together allow extinction probabilities to be computed across the entire domain. On the log scale, regions of loss of information remain, but their locations mirror those observed on the linear scale. In Fig. S1.3a, corresponding to $\log G_{\log}$, the upper-left corner ($w \ll 0$) exhibits a $\text{LOI}_{\text{LOG}0}$ region, which corresponds to the LOI_0 zone of Q_{lin} in Fig. S1.1b. Conversely, in Fig. S1.3b, corresponding to $\log Q_{\log}$, the far right-hand side ($w \gg 0$) contains a $\text{LOI}_{\text{LOG}0}$ region, aligned with the LOI_0 region of G_{lin} in Fig. S1.1a. A grid scan in the log scale over z_{thr} shows that the optimum threshold for minimizing the mean relative error in the hybrid estimation with the Mills approximation is $z_{\text{thr}} \approx 18.5$, which is very close to the linear-scale optimum (Fig. S1.4).

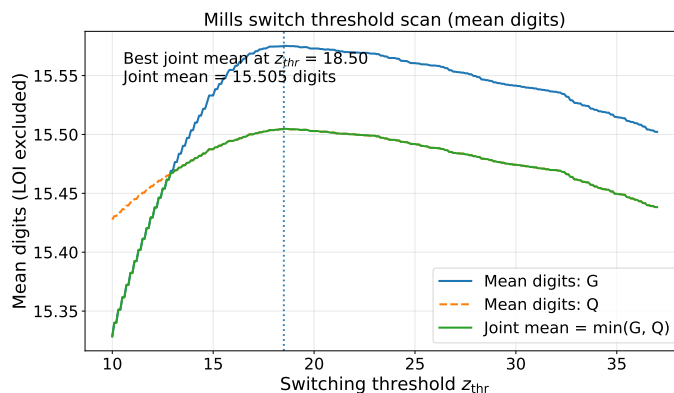


Figure S1.4: Mean digits of accuracy (log scale metric, LOI excluded) versus the z -direction Mills switch threshold z_{thr} ; the vertical dashed line marks the threshold that maximizes the joint mean $\min\{\text{mean}_G, \text{mean}_Q\}$. For the grid and precision used here the optimum occurs near $z_{thr} \approx 18.5$.

Conclusions The linear- and log-scale schemes ($G_{lin}, Q_{lin}, \log G_{log}, \log Q_{log}$) exhibit different relative errors, but all are sufficiently accurate except in regions of loss of information. Fig. S1.5 shows the regions of superiority in the (w, z) domain, with many areas displaying ties. In the left region, where G is difficult to represent in double precision, $\log Q_{log}$ provides stable values, whereas in the right region with analogous challenges, $\log G_{log}$ achieves the highest accuracy. Tie regions, such as $G_{log}|Q_{lin}$ or $G_{lin}|G_{log}|Q_{log}$, occupy broad areas where all schemes perform adequately. Overall, the log scale implementations effectively compensate for the information lost in the linear formulas, demonstrating that logarithmic formulations are robust across the domain. Accordingly, G is evaluated on the linear scale (with the z -direction Mills switch), while probabilities and confidence intervals are reported on the log scale via $\log G$ or $\log Q$ when G is near 0 or 1 to avoid loss of information.

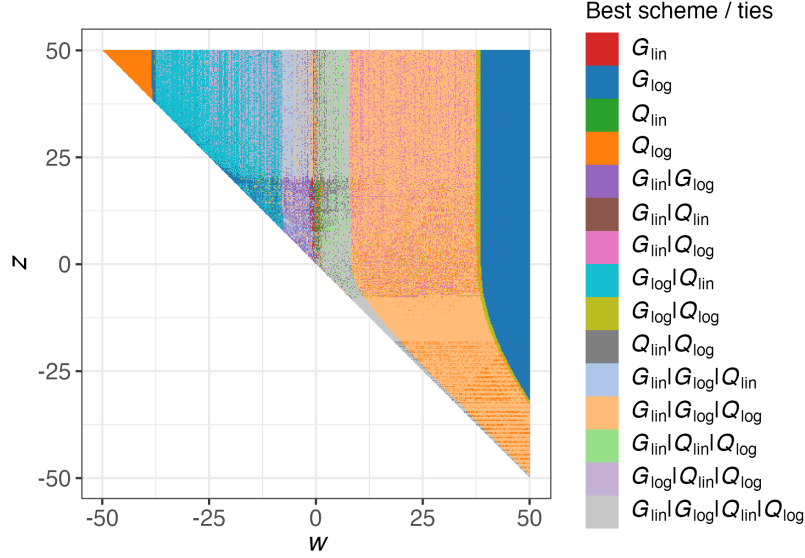


Figure S1.5: Optimal-scheme map comparing numerical accuracy across four evaluation methods for $G(w, z)$ and $Q(w, z)$: G_{lin} , G_{log} , Q_{lin} , and Q_{log} . Each point in the (w, z) domain is colored by the scheme achieving the highest accuracy in digits, with ties grouped into combined categories.

S1.3 Absolute error at the IUCN Criterion E thresholds

While relative error is the natural metric for scanning accuracy over the whole (w, z) domain, Red List category assignments hinge on whether the extinction probability crosses *fixed cut-offs*. In such decision regimes, even a small absolute bias near a threshold can invert the category; absolute error must therefore be evaluated locally around the IUCN Criterion E thresholds $G_{\text{thr}} \in \{0.5, 0.2, 0.1\}$.

To define a symmetric and decision-relevant neighborhood on the probability scale, logit bands are used around each threshold, $|\text{logit}(G_{\text{ref}}) - \text{logit}(G_{\text{thr}})| \leq \log \kappa$ ($\kappa = 1.5$). Within each band, selection is performed on a fixed regular grid in (w, z) with $w \in [-50, 50]$, $z \in [-50, 50]$, step 0.2 on both axes (restricted to $w + z > 0$). Grid points whose MPFR reference satisfies $\text{lo} \leq G_{\text{ref}} < \text{hi}$ are retained, while loss-of-information cases (e.g., linear-scale underflow to 0 or rounding to 1, or non-finite/zero log outputs) are excluded. For the scheme under test, the linear-scale absolute error $|\hat{G} - G_{\text{ref}}|$ is then evaluated at the retained points; for log scale implementations, errors are computed after exponentiating the log outputs. Table S1.2 reports, for each scheme, the sample size N , the maximum, the 95th percentile (p_{95}), and the median absolute error. Across all thresholds and schemes, the worst-case error is $\lesssim 5 \times 10^{-16}$, i.e., on the order of machine epsilon ($\varepsilon \approx 2.2 \times 10^{-16}$) and far below the 10^{-3} – 10^{-2} tolerances commonly

used in Criterion E simulations. Combined with the relative-error results, these bounds are sufficient to guarantee correct CR/EN/VU assignments.

Table S1.2: Absolute-error statistics inside logit bands around the IUCN thresholds. The column “Band [lo, hi]” indicates the probability interval examined.

Threshold	Band [lo, hi]	Scheme	N	max	p_{95}	median
$G_{\text{thr}} = 0.5$	[0.400, 0.600]	G_{lin}	699	3.33×10^{-16}	1.11×10^{-16}	0
		G_{log}	699	5.00×10^{-16}	2.22×10^{-16}	5.55×10^{-17}
		Q_{lin}	699	3.33×10^{-16}	1.11×10^{-16}	5.55×10^{-17}
		Q_{log}	699	4.44×10^{-16}	2.22×10^{-16}	5.55×10^{-17}
$G_{\text{thr}} = 0.2$	[0.143, 0.273]	G_{lin}	561	2.50×10^{-16}	1.39×10^{-16}	2.78×10^{-17}
		G_{log}	561	4.16×10^{-16}	1.67×10^{-16}	2.78×10^{-17}
		Q_{lin}	561	3.33×10^{-16}	1.11×10^{-16}	0
		Q_{log}	561	4.44×10^{-16}	2.22×10^{-16}	0
$G_{\text{thr}} = 0.1$	[0.069, 0.143]	G_{lin}	557	1.94×10^{-16}	5.55×10^{-17}	1.39×10^{-17}
		G_{log}	557	2.22×10^{-16}	1.11×10^{-16}	2.78×10^{-17}
		Q_{lin}	557	2.22×10^{-16}	1.11×10^{-16}	0
		Q_{log}	557	3.33×10^{-16}	1.11×10^{-16}	0

[†] For log scale schemes (G_{log} and Q_{log}), errors are assessed on the linear scale after exponentiation: $G_{\text{log}} = \exp(\log G_{\text{log}})$ and $Q_{\text{log}} = \exp(\log Q_{\text{log}})$.

[‡] For Q schemes, the absolute error is computed directly against $Q_{\text{ref}} = 1 - G_{\text{ref}}$ as $|Q_{\text{scheme}} - Q_{\text{ref}}|$; the quantity $1 - Q_{\text{scheme}}$ is not formed in double precision prior to comparison.

Appendix S2. Monotonicity of $G(w, z)$

This appendix proves that the extinction probability function

$$G(w, z) = \Phi(-w) + \exp\left(\frac{z^2 - w^2}{2}\right) \Phi(-z) \quad \text{for } w + z > 0, \quad w, z \in \mathbb{R} \quad (\text{S2.1})$$

is strictly decreasing in both variables w and z throughout its domain. Here, $\Phi(x)$ denotes the standard normal cumulative distribution function and $\phi(x) = \Phi'(x)$ its corresponding probability density function.

S2.1 Derivative with respect to w

Differentiating Eq. (S2.1) with respect to w gives

$$\begin{aligned} \frac{\partial G}{\partial w} &= \frac{\partial}{\partial w} \Phi(-w) + \frac{\partial}{\partial w} \left[\exp\left(\frac{z^2 - w^2}{2}\right) \right] \Phi(-z), \\ &= -\phi(w) - w \exp\left(\frac{z^2 - w^2}{2}\right) \Phi(-z). \end{aligned} \quad (\text{S2.2})$$

Case 1: $w > 0$. Both terms on the right-hand side of Eq. (S2.2) are negative, so $\partial G/\partial w < 0$ directly.

Case 2: $w < 0$. Because $w + z > 0$, it follows that $z > -w > 0$. Rewrite Eq. (S2.2) as

$$\frac{\partial G}{\partial w} = -\phi(w) + (-w) \exp\left(\frac{z^2 - w^2}{2}\right) \Phi(-z), \quad (-w > 0).$$

Apply the Mills ratio bound (Gordon, 1941)

$$\Phi(-z) < \frac{\phi(z)}{z}, \quad z > 0, \tag{S2.3}$$

and use the identity

$$\exp\left(\frac{z^2 - w^2}{2}\right) \phi(z) = \phi(w). \tag{S2.4}$$

Then

$$(-w) \exp\left(\frac{z^2 - w^2}{2}\right) \Phi(-z) < \frac{-w}{z} \phi(w) < \phi(w),$$

since $-w < z$. Substituting this strict inequality back into the derivative gives

$$\frac{\partial G}{\partial w} < -\phi(w) + \phi(w) = 0.$$

Hence $\partial G/\partial w < 0$ for all $w < 0$ with $w + z > 0$.

S2.2 Derivative with respect to z

Differentiating Eq. (S2.1) with respect to z yields

$$\frac{\partial G}{\partial z} = \exp\left(\frac{z^2 - w^2}{2}\right) [z \Phi(-z) - \phi(z)]. \tag{S2.5}$$

Case 1: $z > 0$. Define the (reciprocal) Mills ratio $M(z) = \Phi(-z)/\phi(z)$, so that Eq. (S2.5) becomes

$$\frac{\partial G}{\partial z} = \exp\left(\frac{z^2 - w^2}{2}\right) \phi(z) [z M(z) - 1].$$

From inequality (S2.3), it follows that $z M(z) < 1$, hence the bracket is negative.

Case 2: $z < 0$. In this case, $z \Phi(-z) < 0$ while $\phi(z) > 0$, so the expression in brackets is again negative.

Therefore, Eq. (S2.5) shows that $\partial G/\partial z < 0$ for all $w + z > 0$.

Remarks at $w = 0$ and $z = 0$. At $w = 0$ one has $\partial G/\partial w = -\phi(0) < 0$. At $z = 0$ one has $\partial G/\partial z = \exp(-(w^2)/2) [0 \cdot \Phi(0) - \phi(0)] < 0$. These confirm strict decrease also on these coordinate axes within $w + z > 0$.

Boundary continuity at $w + z = 0$. On the boundary $z = -w$ one has

$$G(w, -w) = \Phi(-w) + \exp(0) \Phi(w) = \Phi(-w) + \Phi(w) = 1.$$

By continuity of Φ and the exponential, it follows that $G(w, z) \rightarrow 1$ as $w + z \downarrow 0$ with (w, z) restricted to the admissible region $w + z > 0$.

S2.3 Conclusion

The function $G(w, z)$ is strictly decreasing in both w and z throughout its domain:

$$\frac{\partial G}{\partial w}(w, z) < 0 \quad \text{and} \quad \frac{\partial G}{\partial z}(w, z) < 0 \quad \text{for all } w + z > 0. \quad (\text{S2.6})$$

Appendix S3. Asymptotic Behavior of $G(w, z)$ as $z \rightarrow \pm\infty$

The extinction probability from the main text is restated below:

$$G(w, z) = \Phi(-w) + \exp\left(\frac{z^2 - w^2}{2}\right) \Phi(-z) \quad \text{for } w + z > 0, \quad w, z \in \mathbb{R}. \quad (\text{S3.1})$$

This appendix establishes the two limiting forms

$$G(w, z) \simeq \begin{cases} \Phi(-w) & \text{for } z \gg 0, \\ \exp\left(\frac{z^2 - w^2}{2}\right) & \text{for } z \ll 0. \end{cases} \quad (\text{S3.2})$$

and shows that, in the lower-right quadrant ($z < 0, w + z > 0$), the equal-risk contours satisfy $w^2 - z^2 = \text{const}$, with slope $dz/dw = w/z \rightarrow -1$ as $z \rightarrow -\infty$.

Throughout, write $\phi(x) = \Phi'(x) = \frac{1}{\sqrt{2\pi}} \exp(-x^2/2)$ for the standard normal density and recall the Mills ratio bounds (Gordon, 1941)

$$\frac{\phi(x)}{x + 1/x} < \Phi(-x) < \frac{\phi(x)}{x}, \quad x > 0. \quad (\text{S3.3})$$

All limits below are taken with $w + z > 0$.

S3.1 Asymptotics for $z \gg 0$

Consider the second term on the right-hand side of Eq. (S3.1):

$$\exp\left(\frac{z^2 - w^2}{2}\right) \Phi(-z).$$

For $z > 0$, the Mills ratio bound (S3.3) gives

$$\Phi(-z) \leq \frac{\phi(z)}{z}. \quad (\text{S3.4})$$

Hence,

$$\begin{aligned} \exp\left(\frac{z^2 - w^2}{2}\right) \Phi(-z) &\leq \frac{\phi(z)}{z} \exp\left(\frac{z^2 - w^2}{2}\right) \\ &= \frac{1}{z} \cdot \frac{1}{\sqrt{2\pi}} \exp\left(-\frac{w^2}{2}\right) \\ &= \frac{\phi(w)}{z}, \end{aligned} \quad (\text{S3.5})$$

which tends to 0 as $z \rightarrow \infty$ for any fixed w .

To establish that the second term is negligible relative to the first term $\Phi(-w)$, consider the ratio

$$\frac{\exp((z^2 - w^2)/2) \Phi(-z)}{\Phi(-w)} \leq \frac{\phi(w)}{z\Phi(-w)} \rightarrow 0, \quad \text{as } z \rightarrow \infty,$$

because $\Phi(-w)$ is a z -independent positive constant, while the numerator decays like $1/z$.

Therefore, in the limit $z \gg 0$ with fixed w , the second term becomes asymptotically negligible, and

$$G(w, z) \sim \Phi(-w).$$

This establishes the first line of Eq. (S3.2).

S3.2 Asymptotics for $z \ll 0$

Now take the limit $z \rightarrow -\infty$, subject to the constraint $w + z > 0$. Since $z < 0$, it follows that $w > -z$, hence $w > |z|$ and therefore $w \rightarrow \infty$ as $z \rightarrow -\infty$.

In this limit, the first term $\Phi(-w)$ becomes negligible compared to the second. The second term can be written as

$$\exp\left(\frac{z^2 - w^2}{2}\right) \Phi(-z) = \exp\left(\frac{z^2 - w^2}{2}\right) \left[1 + O\left(\frac{\phi(|z|)}{|z|}\right)\right],$$

using that $\Phi(-z) = 1 - \Phi(z)$ and $\Phi(z) = O(\phi(|z|)/|z|)$ as $z \rightarrow -\infty$.

For the first term, the Mills bound implies

$$\Phi(-w) = O\left(\frac{\phi(w)}{w}\right) = O\left(\frac{e^{-w^2/2}}{w}\right), \quad w \rightarrow \infty.$$

Hence, the ratio of the first term to the second is

$$\frac{\Phi(-w)}{\exp((z^2 - w^2)/2)} = O\left(\frac{e^{-w^2/2}}{w}\right) e^{(w^2 - z^2)/2} = O\left(\frac{e^{-z^2/2}}{w}\right) \rightarrow 0,$$

as $z \rightarrow -\infty$.

It follows that the first term is negligible, and

$$G(w, z) \sim \exp\left(\frac{z^2 - w^2}{2}\right), \quad z \rightarrow -\infty.$$

This completes the proof of the second line of Eq. (S3.2).

S3.3 Asymptotic form of equal-risk contours for $z \ll 0$

Fix $G(w, z) = c \in (0, 1)$ in the region $z < 0$ and $w + z > 0$. Applying the asymptotic approximation derived in the previous subsection for $z \ll 0$ yields

$$c = \exp\left(\frac{z^2 - w^2}{2}\right) + o(1) \implies w^2 - z^2 = -2 \log c + o(1).$$

Differentiating the level set $w^2 - z^2 = \text{const}$ with respect to w gives

$$2w dw - 2z dz = 0 \implies \frac{dz}{dw} = \frac{w}{z}.$$

In the domain $z < 0$ and $w > |z|$, it follows that $w/z < 0$ and $|w/z| > 1$. Hence,

$$\frac{dz}{dw} = \frac{w}{z} = -\left|\frac{w}{z}\right| < -1 \quad \text{and} \quad \frac{dz}{dw} \rightarrow -1 \quad \text{as} \quad z \rightarrow -\infty,$$

Therefore, the equal-risk contours are steeper than the diagonal line $w = -z$ and approach it asymptotically from below.

Remark. For $z \rightarrow +\infty$,

$$G(w, z) = \Phi(-w) + \frac{\phi(w)}{z} \left(1 - \frac{1}{z^2} + O(z^{-4})\right).$$

Thus the one-term approximation $G \simeq \Phi(-w)$ has relative error $O(1/z)$, while including the next term $G \simeq \Phi(-w) + \phi(w)/z$ reduces the residual relative error to $O(1/z^2)$. For $z \rightarrow -\infty$ with $w + z > 0$, since $\Phi(-z) = 1 - O(\phi(|z|)/|z|)$ and $\Phi(-w)$ is exponentially smaller than $\exp((z^2 - w^2)/2)$, the approximation $G \simeq \exp((z^2 - w^2)/2)$ has relative error $O(\phi(|z|)/|z|) = O(e^{-z^2/2}/|z|)$, i.e., exponentially small. These accuracies ensure that the asymptotic forms are highly reliable even for moderate values of $|z|$, and hence suitable for use in the CI construction in Section 4.

Appendix S4. Slope of Equal-Risk Contours for $w + z > 0$

This appendix shows that the equal-risk contours $G(w, z) = c$ in the region $w + z > 0$ are steeper than the diagonal line $w = -z$.

The extinction-probability function under analysis is restated below:

$$G(w, z) = \Phi(-w) + \exp\left(\frac{z^2 - w^2}{2}\right) \Phi(-z) \quad \text{for } w + z > 0, \quad w, z \in \mathbb{R}. \quad (\text{S4.1})$$

Here, $\Phi(x)$ denotes the standard normal cumulative distribution function and $\phi(x) = \Phi'(x)$ is the corresponding probability density function.

Implicit differentiation of $G(w, z) = c$ gives the slope

$$\frac{dz}{dw} = -\frac{\partial G/\partial w}{\partial G/\partial z} = -\frac{G_w}{G_z} = \frac{\phi(z) + w \Phi(-z)}{z \Phi(-z) - \phi(z)} =: S(w, z). \quad (\text{S4.2})$$

S4.1 Auxiliary function

Define

$$h(z) := \phi(z) - z \Phi(-z), \quad (\text{S4.3})$$

where ϕ and Φ denote the standard normal density and distribution function, respectively.

Since $\phi'(z) = -z \phi(z)$ and $\Phi'(-z) = -\phi(z)$, it follows that

$$h'(z) = -\Phi(-z) < 0 \quad \text{for all } z \in \mathbb{R},$$

so $h(z)$ is strictly decreasing.

To establish that $h(z) > 0$ for all z , consider first the case $z < 0$. In this region, both $\phi(z)$ and $\Phi(-z)$ are positive, and the negative sign on z implies that $-z \Phi(-z) > 0$, so $h(z) = \phi(z) + |z| \Phi(-z) > 0$. On the other hand, for $z \geq 0$, the Mills upper bound $\Phi(-z) < \phi(z)/z$ (Gordon, 1941) yields

$$z \Phi(-z) < \phi(z) \quad \implies \quad h(z) = \phi(z) - z \Phi(-z) > 0.$$

Therefore $h(z)$ is strictly positive for all $z \in \mathbb{R}$, strictly decreasing in z , and satisfies $\lim_{z \rightarrow +\infty} h(z) = 0$ and $\lim_{z \rightarrow -\infty} h(z) = +\infty$.

S4.2 Comparison with the diagonal

To compare $S(w, z)$ with -1 , multiply both sides of $S(w, z) < -1$ by the negative denominator $z \Phi(-z) - \phi(z) = -h(z)$:

$$\begin{aligned} S(w, z) < -1 &\iff (\phi(z) + w \Phi(-z)) + (z \Phi(-z) - \phi(z)) > 0 \\ &\iff \Phi(-z)(w + z) > 0. \end{aligned} \quad (\text{S4.4})$$

Because $\Phi(-z) > 0$ and $w + z > 0$, the inequality holds, yielding

$$\frac{dz}{dw} = S(w, z) < -1 \quad \text{throughout the region } w + z > 0. \quad (\text{S4.5})$$

Therefore the equal-risk contours are strictly steeper than the diagonal $w = -z$ across the entire domain $w + z > 0$.

Appendix S5. Details of the Sampling Correlation of \hat{w} and \hat{z}

This appendix outlines the derivation of the closed-form expression for the correlation coefficient between the estimators \hat{w} and \hat{z} .

S5.1 Definition of w and z and their estimators

Consider two mutually independent random variables $\hat{\mu}$ and $\hat{\sigma}^2$, which satisfy

$$\hat{\mu} \sim \mathcal{N}\left(\mu, \frac{\sigma^2}{t_q}\right), \quad \frac{q\hat{\sigma}^2}{\sigma^2} \sim \chi_{q-1}^2,$$

and serve as estimators of the drift $\mu \in \mathbb{R}$ and the variance $\sigma^2 > 0$ of the Wiener process with drift. Suppose that observations are available at q intervals over a total observation time span $t_q > 0$.

For any $t > 0$ and initial log-distance $x_d > 0$, define

$$w = \frac{\mu t + x_d}{\sigma\sqrt{t}}, \quad z = \frac{-\mu t + x_d}{\sigma\sqrt{t}}.$$

For inference at a finite time horizon t^* , the plug-in estimators are

$$\hat{w} = \frac{\hat{\mu} t^* + x_d}{\hat{\sigma}\sqrt{t^*}}, \quad \hat{z} = \frac{-\hat{\mu} t^* + x_d}{\hat{\sigma}\sqrt{t^*}}.$$

S5.2 Reparameterization and auxiliary variables

It is convenient to introduce the reparameterization

$$m := t^*\hat{\mu}, \quad \eta := \hat{\sigma}^{-1}, \quad \bar{m} := \mathbb{E}[m] = t^*\mu, \quad \sigma_m^2 := \text{Var}(m) = \frac{t^{*2}\sigma^2}{t_q}.$$

Then $m \sim \mathcal{N}(\bar{m}, \sigma_m^2)$. Since $\hat{\mu}$ and $\hat{\sigma}^2$ are independent, it follows that m and η are independent (as functions of independent variables), and

$$\hat{w} = \frac{x_d + m}{\sqrt{t^*}} \eta, \quad \hat{z} = \frac{x_d - m}{\sqrt{t^*}} \eta.$$

Moments of $\eta = \hat{\sigma}^{-1}$. Write $Y := q\hat{\sigma}^2/\sigma^2 \sim \chi_\nu^2$ with $\nu = q - 1$. Then

$$\eta = \hat{\sigma}^{-1} = \frac{1}{\sigma} \sqrt{\frac{q}{Y}}.$$

For a chi-squared random variable $Y \sim \chi_\nu^2$ with ν degrees of freedom, the following identity for inverse moments holds whenever $a < \nu/2$:

$$\mathbb{E}[Y^{-a}] = 2^{-a} \frac{\Gamma(\frac{\nu}{2} - a)}{\Gamma(\frac{\nu}{2})}.$$

Applying this formula yields, for $q > 2$ (for $\mathbb{E}[\eta]$) and $q > 3$ (for $\mathbb{E}[\eta^2]$),

$$\mathbb{E}[\eta] = \frac{\sqrt{q}}{\sqrt{2}\sigma} \frac{\Gamma((q-2)/2)}{\Gamma((q-1)/2)}, \quad \mathbb{E}[\eta^2] = \frac{q}{(q-3)\sigma^2}.$$

Hence

$$\sigma_\eta^2 := \text{Var}(\eta) = \frac{q}{\sigma^2} \left[\frac{1}{q-3} - \frac{1}{2} \left\{ \frac{\Gamma((q-2)/2)}{\Gamma((q-1)/2)} \right\}^2 \right], \quad q > 3.$$

The following formulas require $q > 2$ (for $\mathbb{E}[\eta]$) and for $q > 3$ (for $\mathbb{E}[\eta^2]$ and $\text{Var}(\eta)$).

S5.3 Variances and covariance of (\hat{w}, \hat{z})

Using independence of m and η and elementary identities for moments of products,

$$\begin{aligned} \text{Var}(\hat{w}) &= \frac{\mathbb{E}[\eta^2] \sigma_m^2 + \sigma_\eta^2 (x_d + \bar{m})^2}{t^*}, & \text{Var}(\hat{z}) &= \frac{\mathbb{E}[\eta^2] \sigma_m^2 + \sigma_\eta^2 (x_d - \bar{m})^2}{t^*}, \\ \text{Cov}(\hat{w}, \hat{z}) &= \frac{-\mathbb{E}[\eta^2] \sigma_m^2 + \sigma_\eta^2 (x_d^2 - \bar{m}^2)}{t^*}. \end{aligned}$$

S5.4 Closed-form correlation

Using

$$x_d = \frac{\sigma\sqrt{t^*}}{2} (w + z), \quad \bar{m} = \frac{\sigma\sqrt{t^*}}{2} (w - z),$$

one has

$$(x_d + \bar{m})^2 = \sigma^2 t^* w^2, \quad (x_d - \bar{m})^2 = \sigma^2 t^* z^2, \quad x_d^2 - \bar{m}^2 = \sigma^2 t^* w z.$$

Introduce the design-dependent constants

$$A := \mathbb{E}[\eta^2] \sigma_m^2 = \frac{q t^{*2}}{(q-3) t_q}, \quad D := \sigma_\eta^2 \sigma^2 t^* = q t^* \left[\frac{1}{q-3} - \frac{1}{2} \left\{ \frac{\Gamma((q-2)/2)}{\Gamma((q-1)/2)} \right\}^2 \right],$$

which depend only on (q, t_q, t^*) and not on (μ, σ, x_d) . Then

$$\text{Var}(\widehat{w}) = \frac{A + D w^2}{t^*}, \quad \text{Var}(\widehat{z}) = \frac{A + D z^2}{t^*}, \quad \text{Cov}(\widehat{w}, \widehat{z}) = \frac{-A + D w z}{t^*},$$

and therefore, for $w + z > 0$,

$$\text{Corr}(\widehat{w}, \widehat{z}) = \frac{-A + D w z}{\sqrt{(A + D w^2)(A + D z^2)}}.$$

Defining $k := A/D$ yields

$$\text{Corr}(\widehat{w}, \widehat{z}) = \frac{-k + w z}{\sqrt{(k + w^2)(k + z^2)}}, \quad w + z > 0, \quad k > 0. \quad (\text{S5.1})$$

S5.5 Positivity of D and k

Let

$$r_q := \frac{\Gamma((q-2)/2)}{\Gamma((q-1)/2)}, \quad q > 3.$$

Gautschi's inequality states that for $x > 0$ and $0 < s < 1$,

$$x^{1-s} < \frac{\Gamma(x+1)}{\Gamma(x+s)} < (x+1)^{1-s}.$$

Applying it with $s = \frac{1}{2}$ and $x = (q-3)/2$ gives

$$\frac{1}{\sqrt{x+1}} < \frac{\Gamma(x+\frac{1}{2})}{\Gamma(x+1)} < \frac{1}{\sqrt{x}},$$

and therefore

$$r_q^2 < \frac{2}{q-3}.$$

Hence

$$\frac{1}{q-3} - \frac{1}{2} r_q^2 > 0,$$

so $D > 0$. Since $A > 0$ trivially, $k = A/D > 0$ whenever $q > 3$, $t_q > 0$, and $t^* > 0$.

S5.6 Asymptotic behavior of k and parameter dependence

Using the Stirling-type expansion for the Gamma ratio,

$$\frac{\Gamma((q-2)/2)}{\Gamma((q-1)/2)} = \sqrt{\frac{2}{q-1}} (1 + O(q^{-1})),$$

one obtains

$$A = \frac{q t^{*2}}{(q-3) t_q} = \frac{t^{*2}}{t_q} (1 + O(q^{-1})),$$

and

$$D = q t^* \left[\frac{1}{q-3} - \frac{1}{2} \left\{ \frac{\Gamma((q-2)/2)}{\Gamma((q-1)/2)} \right\}^2 \right] = \frac{t^*}{2q} (1 + O(q^{-1})).$$

Consequently,

$$k = \frac{A}{D} = \frac{2q t^*}{t_q} (1 + O(q^{-1})),$$

so k grows linearly with q up to $O(q^{-1})$ corrections, and is exactly proportional to t^* and inversely proportional to t_q .

S5.7 Geometric implications

On the admissible half-plane $w + z > 0$, the correlation landscape in (S5.1) has the following features. In the first quadrant ($w, z > 0$), the sign changes on the hyperbola $wz = k$: outside this curve the correlation is positive, and inside it is negative. Along the axes ($w = 0$ or $z = 0$), the correlation is strictly negative and tends to 0 as the other coordinate diverges, reflecting the fact that the curve $wz = k$ is asymptotic to the axes. For $wz < 0$ the correlation is negative throughout. Moreover, if both $|w|$ and $|z|$ grow without bound (e.g., $w = ta$, $z = tb$ with $t \rightarrow \infty$ for fixed a, b), then

$$\text{Corr}(\hat{w}, \hat{z}) \longrightarrow \begin{cases} +1, & \text{when } w \text{ and } z \text{ have the same sign,} \\ -1, & \text{when } w \text{ and } z \text{ have opposite signs.} \end{cases}$$

Appendix S6. Monte Carlo evaluation of confidence interval methods

S6.1 Monte Carlo procedure

Recall that the extinction probability is defined by

$$\begin{aligned} \Pr[T \leq t \mid x_d, \mu, \sigma^2] &= G(t \mid x_d, \mu, \sigma^2) \\ &= G(w, z) \\ &= \Phi(-w) + \exp\left(\frac{z^2 - w^2}{2}\right) \Phi(-z) \quad \text{for } w + z > 0, \quad w, z \in \mathbb{R}, \end{aligned}$$

where $w = (\mu t + x_d)/\sigma\sqrt{t}$ and $z = (-\mu t + x_d)/\sigma\sqrt{t}$ are transformed parameters. With $t = t^*$, the finite time horizon for extinction risk prediction, the ML estimators from Eq. (8) yield transformed statistics \hat{w}, \hat{z} . Independent random variables $\hat{\mu}$ and $\hat{\sigma}^2$ were generated according to their exact sampling distributions under observation span $t_q = q$:

$$\hat{\mu} \sim N(\mu, \sigma^2/t_q), \quad \hat{\sigma}^2 \sim \frac{\sigma^2}{q} \chi_{q-1}^2.$$

Each replicate pair $(\hat{\mu}, \hat{\sigma}^2)$ was substituted into the definitions

$$\hat{w} = \frac{\hat{\mu}t^* + x_d}{\hat{\sigma}\sqrt{t^*}}, \quad \hat{z} = \frac{-\hat{\mu}t^* + x_d}{\hat{\sigma}\sqrt{t^*}},$$

and then used to compute $G(\hat{w}, \hat{z})$ and the confidence intervals for each method.

Numerical evaluation. The function G was evaluated using a log-stable implementation described in Appendix S1. Specifically, sums and differences on the probability scale were computed on the log scale via log-sum-exp and log-difference identities; the factor $(z^2 - w^2)/2$ was formed as $((z + w)(z - w))/2$ to reduce cancellation; and an eight-term Mills expansion in the z -direction was applied beyond a threshold $z_{\text{thr}} = 19$ to avoid overflow and loss of precision. In regions where G is numerically ill-conditioned (notably $w \ll 0$ with $G \rightarrow 1$), the complementary probability $Q = 1 - G$ was evaluated for the coverage decision and recorded alongside G (“ G -for- Q ” hybrid); the switching rule was fixed per parameter cell (based on the true parameters) and never per replicate. All methods were applied to identical sets of replicate statistics to ensure comparability of results.

In this way, Monte Carlo replicates of the extinction probability and its confidence intervals were obtained without simulating full time series.

S6.2 Confidence interval methods

Confidence intervals for G were evaluated using four methods: the w - z method, the theoretical minimum uncertainty (TMU) CI, the delta/logit method, and the percentile bootstrap. The latter three methods are described below.

S6.2.1 Theoretical minimum uncertainty (TMU) CI

The TMU confidence interval (Fieberg & Ellner, 2000; Ellner & Holmes, 2008) assumes that the environmental variance σ^2 is known and ignores uncertainty in its estimation. Writing extinction risk as

$$G(w, z) = \Phi(U - V) + \exp(2UV) \Phi(-(U + V)),$$

where $U = -\mu\sqrt{t^*}/\sigma$ and $V = x_d/(\sigma\sqrt{t^*})$, the TMU interval for q increments takes the form

$$G(\hat{U} - z_{\alpha/2}\sqrt{t^*/q}, \hat{V}) \leq G \leq G(\hat{U} + z_{\alpha/2}\sqrt{t^*/q}, \hat{V}).$$

This construction perturbs only the U component, corresponding to growth rate uncertainty, while V is treated as fixed. In the limit of large V , the expression reduces to a simple probit shift, $\Phi^{-1}(\hat{G}) \pm z_{\alpha/2}\sqrt{t^*/q}$. Because variance uncertainty is excluded, the TMU interval is generally anti-conservative, and Monte Carlo validation shows empirical rejection rates that often exceed the nominal level.

S6.2.2 Delta/logit method

The delta/logit method (Dennis *et al.*, 1991) applies a first-order delta approximation to the logit of the extinction probability. Let

$$H(t \mid x_d, \mu, \sigma^2) = \log \left(\frac{G(t \mid x_d, \mu, \sigma^2)}{1 - G(t \mid x_d, \mu, \sigma^2)} \right).$$

The variance of $\hat{H} = H(t \mid x_d, \hat{\mu}, \hat{\sigma}^2)$ is approximated as

$$\begin{aligned} \text{Var}(\hat{H}) &\approx \left(\frac{\partial H}{\partial \mu} \right)^2 \text{Var}(\hat{\mu}) + \left(\frac{\partial H}{\partial \sigma^2} \right)^2 \text{Var}(\hat{\sigma}^2), \\ &= \left(\frac{\partial G / \partial \mu}{G(1 - G)} \right)^2 \text{Var}(\hat{\mu}) + \left(\frac{\partial G / \partial \sigma^2}{G(1 - G)} \right)^2 \text{Var}(\hat{\sigma}^2), \end{aligned}$$

with

$$\text{Var}(\hat{\mu}) = \frac{\sigma^2}{t_q} = \frac{\sigma^2}{q}, \quad \text{Var}(\hat{\sigma}^2) = \frac{2\sigma^4(q-1)}{q^2}.$$

The derivatives are

$$\begin{aligned} \frac{\partial G}{\partial \mu} &= -\frac{2x_d}{\sigma^2} \exp\left(\frac{z^2 - w^2}{2}\right) \Phi(-z), \\ \frac{\partial G}{\partial \sigma^2} &= \frac{x_d}{\sigma^3\sqrt{t^*}} \phi(w) + \frac{2\mu x_d}{\sigma^4} \exp\left(\frac{z^2 - w^2}{2}\right) \Phi(-z). \end{aligned}$$

The two-sided Wald interval on the logit scale, $\widehat{H} \pm z_{\alpha/2} \sqrt{\text{Var}(\widehat{H})}$, is mapped back to the probability scale by the inverse logit.

Implementation details. The evaluation of G and its derivatives was carried out on the log scale using stable transforms, with the same Mills expansion as in Appendix S1, in order to avoid underflow or cancellation. Despite these precautions, the delta/logit method remains sensitive in extreme regions ($w \ll 0$ or $w \gg 0$), where G or Q approaches the limits of double precision. In Monte Carlo experiments this method often yields empirical rejection rates below the nominal level in some regions and above it in others, reflecting the limitations of a first-order linearization.

S6.2.3 Percentile parametric bootstrap

The percentile parametric bootstrap treats $(\widehat{\mu}, \widehat{\sigma}^2)$ as plug-in truths and draws independent bootstrap replicates from their sampling laws with span $t_q = q$:

$$\mu^{(b)} \sim N\left(\widehat{\mu}, \frac{\widehat{\sigma}^2}{t_q}\right), \quad \sigma^{2(b)} \sim \frac{\widehat{\sigma}^2}{q} \chi_{q-1}^2.$$

For each draw, the extinction probability is recomputed as

$$G^{(b)} = G\left(\frac{\mu^{(b)}t^* + x_d}{\sigma^{(b)}\sqrt{t^*}}, \frac{-\mu^{(b)}t^* + x_d}{\sigma^{(b)}\sqrt{t^*}}\right).$$

After B replicates, the percentile interval is

$$\text{CI}_G^{\text{PPB}} = [G_{(\lceil(\alpha/2)B\rceil)}, G_{(\lceil(1-\alpha/2)B\rceil)}],$$

where $G_{(k)}$ is the k th order statistic of $\{G^{(b)}\}_{b=1}^B$.

Typical runs used $B = 2,000$, which provides sufficient resolution for the percentile estimates while keeping computation time moderate. Additional checks with larger values ($B = 5,000$ – $10,000$) yielded essentially identical results, indicating that $B = 2,000$ is adequate for stable estimation. All bootstrap evaluations of G were carried out using the log-stable implementation described in Appendix S1, so that very small or very large probabilities were handled without numerical underflow or loss of precision.

S6.3 Evaluation metric

For each parameter combination, $N = 10,000$ replicates were generated. The empirical rejection rate (that is, one minus the coverage probability) was computed as the proportion of replicates in which the true G was not contained in the estimated CI. The binomial standard error of this estimate is at most 0.005 for the reported ranges.

S6.4 Implementation notes

Evaluation of $G(w, z)$ relied on log-scale formulas and an 8-term Mills expansion for large z values; details are provided in Appendix S1. Noncentral- t inversions for the w - z method used bracketing solvers with tolerance 10^{-10} . All methods were applied to identical sets of replicate statistics to ensure comparability of results.

A bias-corrected and accelerated (BCa) bootstrap was also tested in preliminary runs (see Efron & Tibshirani, 1993). Although mean rejection rates were marginally lower than those of the percentile bootstrap, the BCa intervals exhibited greater variability with occasional extreme outliers, and remained anti-conservative overall. For this reason, BCa results are not reported in the main text.

Appendix S7. Confidence-interval width as a function of data and model parameters

This appendix analyzes how the confidence interval for the extinction probability depends on the data and on the model parameters. Although $G(t | \cdot)$ is defined for arbitrary $t > 0$, in what follows I fix $t = t^*$, a finite time horizon for extinction risk assessment, so that the distribution of its estimator unavoidably depends on t^* . Although G is defined only in terms of the transformed parameters (w, z) , the distribution of its estimator unavoidably depends on the time horizon t^* . The aim is to disentangle these contributions and to describe the asymptotic behavior of the interval across different regions of the (w, z) plane. Two complementary approaches are used: the delta method, which provides an analytically transparent quadratic-form decomposition linking sampling design and model sensitivity under large-sample asymptotic normality, and a mixture representation, which yields more accurate results at finite q . In particular, the mixture approach gives semi-exact formulas in the region $z > 0$, while the delta method remains useful for structural interpretation across the full domain.

S7.1 Setup and definitions

I first recall the relevant definitions. For any $t > 0$ and initial log-distance $x_d > 0$, define

$$w = \frac{\mu t + x_d}{\sigma \sqrt{t}}, \quad z = \frac{-\mu t + x_d}{\sigma \sqrt{t}}.$$

The extinction probability in transformed coordinates was defined in Eq. (6) of the main text as

$$G(w, z) = \Phi(-w) + \exp\left(\frac{z^2 - w^2}{2}\right) \Phi(-z), \quad w + z > 0,$$

with gradient components (Appendix S2)

$$\frac{\partial G}{\partial w} = G_w = -\phi(w) - w \exp\left(\frac{z^2 - w^2}{2}\right) \Phi(-z), \quad \frac{\partial G}{\partial z} = G_z = \exp\left(\frac{z^2 - w^2}{2}\right) (z\Phi(-z) - \phi(z)).$$

Throughout, Φ and ϕ denote the standard normal distribution and density.

For inference at a fixed finite time horizon t^* , the plug-in estimators are

$$\widehat{w} = \frac{\widehat{\mu} t^* + x_d}{\widehat{\sigma} \sqrt{t^*}}, \quad \widehat{z} = \frac{-\widehat{\mu} t^* + x_d}{\widehat{\sigma} \sqrt{t^*}}, \quad q > 1,$$

where $\widehat{\mu}$ and $\widehat{\sigma}^2$ are mutually independent, a property specific to the normal model (Subsection 4.1). As established in Subsection 4.2, these follow noncentral- t distributions with $q - 1$ degrees of freedom:

$$\widehat{w} \sqrt{\frac{q-1}{q}} \sqrt{\frac{t_q}{t^*}} \sim t\left(w \sqrt{\frac{t_q}{t^*}}, q - 1\right), \quad \widehat{z} \sqrt{\frac{q-1}{q}} \sqrt{\frac{t_q}{t^*}} \sim t\left(z \sqrt{\frac{t_q}{t^*}}, q - 1\right).$$

Their joint covariance structure, derived in Subsection 4.2 and Appendix S5, is

$$\Sigma = c(q) \begin{pmatrix} k + w^2 & -k + wz \\ -k + wz & k + z^2 \end{pmatrix}, \quad (\text{S7.1})$$

where $c(q)$ depends only on the sample size (minus one) q , while k depends on (q, t_q, t^*) :

$$c(q) = \frac{D}{t^*} = q \left[\frac{1}{q-3} - \frac{1}{2} \left\{ \frac{\Gamma((q-2)/2)}{\Gamma((q-1)/2)} \right\}^2 \right] > 0,$$

$$k(q, t_q, t^*) = \frac{t^*}{t_q} \left[1 - \frac{1}{2}(q-3) \left\{ \frac{\Gamma((q-2)/2)}{\Gamma((q-1)/2)} \right\}^2 \right]^{-1} > 0, \quad q > 3.$$

From this structure, Appendix S5 also showed that

$$\text{Corr}(\widehat{w}, \widehat{z}) = \rho(w, z; k) = \frac{-k + wz}{\sqrt{(k + w^2)(k + z^2)}}.$$

Remark on the roles of q and t_q . From Eq. (10) one has $\widehat{\mu} \sim \mathcal{N}(\mu, \sigma^2/t_q)$, so $\text{Var}(\widehat{\mu})$ decreases in proportion to $1/t_q$ and is independent of q . Thus increasing q primarily stabilizes $\widehat{\sigma}^2$ and raises the degrees of freedom in the noncentral- t laws for $(\widehat{w}, \widehat{z})$, while increasing t_q directly improves the signal for $\widehat{\mu}$. Equivalently, in the notation of (S7.1), $c(q) \sim 1/q$ but $c(q) k(q, t_q, t^*) = \frac{q}{q-3} \frac{t^*}{t_q}$, so with t_q fixed the leading entries of Σ converge to t^*/t_q as $q \rightarrow \infty$, explaining the plateau in CI width; extending t_q lowers this plateau.

S7.2 Delta-method expression

Let $\widehat{G} = G(\widehat{w}, \widehat{z})$ be the estimator of the extinction probability. Under large-sample asymptotics in q (with t^* and t_q fixed),

$$(\widehat{w} - w, \widehat{z} - z)^\top \Rightarrow \mathcal{N}(0, \Sigma(q, t_q, t^*)).$$

By the delta method, which applies under this asymptotic normality,

$$\text{Var}(\widehat{G}) \approx \nabla G(w, z)^\top \Sigma \nabla G(w, z), \quad (\text{S7.2})$$

where $\nabla G(w, z) = (G_w, G_z)^\top$ and Σ is given in (S7.1). Hence the half-width of the two-sided $100(1 - \alpha)\%$ Wald interval is

$$h_G(w, z) = z_{1-\alpha/2} \|\nabla G(w, z)\|_\Sigma, \quad (\text{S7.3})$$

with $\|v\|_\Sigma = \sqrt{v^\top \Sigma v}$. Explicitly,

$$\|\nabla G(w, z)\|_\Sigma^2 = G_w^2 \Sigma_{11} + 2G_w G_z \Sigma_{12} + G_z^2 \Sigma_{22}.$$

Thus both the data (q, t_q) and the model parameters (w, z, t^*) enter through Σ , while the sensitivity of G itself contributes through the gradient components G_w, G_z . As $G \rightarrow 0$ or $G \rightarrow 1$, both G_w and G_z vanish, so that $h_G \rightarrow 0$.

For moderate $z > 0$, the approximation $G \simeq \Phi(-w)$ yields $\nabla G \simeq (-\phi(w), 0)^\top$ and thus

$$\|\nabla G(w, z)\|_\Sigma^2 \simeq \phi(w)^2 \Sigma_{11} = c(q) \phi(w)^2 (k + w^2).$$

In this approximation the squared width satisfies

$$h_G^2 \propto \phi(w)^2 (k + w^2) = \frac{1}{2\pi} e^{-w^2} (k + w^2).$$

Maximizing $e^{-w^2} (k + w^2)$ with respect to w therefore determines the point of maximal interval width. The maximum occurs at $w = 0$ when $k \geq 1$, whereas for $0 < k < 1$ it is attained at $w = \pm\sqrt{1-k}$, because $e^{-(1-k)} > k$ for $0 < k < 1$. This two-hump structure for $k < 1$ is clearly seen in finite- q calculations; see Fig. S7.1c (note that for $z < 0$ no such splitting occurs; cf. Fig. S7.1d). In typical applications k scales like $q(t^*/t_q)$ and is usually ≥ 1 , so the maximal width occurs at $w = 0$, i.e., at intermediate extinction probability ($G \simeq 0.5$) in this regime.

In the opposite tail, $z \ll 0$, the extinction probability behaves as $G(w, z) \approx \exp((z^2 - w^2)/2)$, and its gradient as $\nabla G(w, z) \approx (-wG, zG)^\top$. Substitution into (S7.3) then yields

$$h_G \approx z_{1-\alpha/2} \sqrt{c(q)} G \sqrt{(w^2 - z^2)^2 + k(q, t_q, t^*) (w + z)^2}.$$

Introducing $\kappa = w + z > 0$ as the distance from the boundary and writing $w = \kappa - z$ gives

$$G = \exp\left(\kappa z - \frac{\kappa^2}{2}\right),$$

so for fixed κ the width h_G decays exponentially in $|z|$, with only polynomial modulation from the square-root factor involving $c(q)$ and $k(q, t_q, t^*)$. No interior maximum arises in this regime.

Upper bound and overestimation. Since $\widehat{G} \in [0, 1]$, its variance is bounded by $1/4$ regardless of the parameter values. In the $z > 0$ regime where $G \simeq \Phi(-w)$, the delta-method variance attains

$$\max_w \text{Var}_\Delta(\widehat{G}) = \begin{cases} \frac{c(q)}{2\pi} k, & \text{attained at } w = 0 \text{ when } k \geq 1, \\ \frac{c(q)}{2\pi} e^{-(1-k)}, & \text{attained at } w = \pm\sqrt{1-k} \text{ when } 0 < k < 1. \end{cases}$$

using the identity $c(q)k = (q/(q-3))(t^*/t_q)$. Therefore, for $k \geq 1$, whenever

$$\frac{q}{q-3} \frac{t^*}{t_q} > \frac{\pi}{2},$$

its maximal value necessarily exceeds the universal upper bound $1/4$, implying overestimation of the true variance and the corresponding CI width. At the symmetry point $w = 0$ and in the large- q limit, the delta variance is $\text{Var}_\Delta(\widehat{G}) \rightarrow \frac{1}{2\pi} \frac{t^*}{t_q}$, whereas the mixture (true) variance (see next subsection) is $\text{Var}_{\text{mix}}(\widehat{G}) \rightarrow \frac{1}{2\pi} \arcsin\left(\frac{t^*/t_q}{1+t^*/t_q}\right)$. Since $\frac{t^*}{t_q} > \arcsin\left(\frac{t^*/t_q}{1+t^*/t_q}\right)$ for all $t^*/t_q > 0$, the delta method overestimates the variance at $w = 0$ for any $t^*/t_q > 0$.

In the opposite tail ($z \ll 0$), $G(w, z) \approx \exp((z^2 - w^2)/2)$ decays exponentially, and both the delta and true variances are proportional to G^2 up to polynomial factors in (w, z) ; hence no systematic overestimation arises.

In contrast, as $G \rightarrow 0$ or $G \rightarrow 1$ both gradient components vanish, so that $\text{Var}_\Delta(\widehat{G}) \rightarrow 0$ consistently with the true variance. Thus the overestimation phenomenon is confined to the central $z > 0$ region, where $G \simeq \Phi(-w)$ and the delta method can exceed the variance bound.

For completeness, in the $0 < k < 1$ branch the maximum is $\frac{c(q)}{2\pi} e^{-(1-k)} < \frac{c(q)}{2\pi}$; since $\frac{c(q)}{2\pi} < \frac{1}{4}$ for all $q \geq 4$, the upper-bound argument above does not apply (the delta method need not overestimate).

S7.3 Mixture representation

Although the variance of $\widehat{G} = G(\widehat{w}, \widehat{z})$ can in principle be expressed as a two-dimensional integral over the joint distribution of $(\widehat{w}, \widehat{z})$, the density is intractable. A more convenient approach uses the standard mixture representation of noncentral t statistics.

As introduced in Appendix S5, the estimators can be written as

$$\widehat{w} = \frac{x_d + m}{\sqrt{t^*}} \eta, \quad \widehat{z} = \frac{x_d - m}{\sqrt{t^*}} \eta,$$

where $m = t^* \widehat{\mu}$ and $\eta = \widehat{\sigma}^{-1}$ are independent. It is convenient to set

$$m = \bar{m} + \sigma_m Z, \quad Z \sim \mathcal{N}(0, 1), \quad \bar{m} = t^* \mu, \quad \sigma_m^2 = t^{*2} \sigma^2 / t_q,$$

and introduce

$$s = \sqrt{t^*/t_q}, \quad \Lambda = \sigma\eta = \sqrt{q/\chi_{q-1}^2}, \quad Z \sim \mathcal{N}(0, 1) \text{ and } Z \perp\!\!\!\perp \Lambda.$$

Then the estimators admit the mixture representation in terms of a standard normal $Z \sim \mathcal{N}(0, 1)$ and an independent random scale Λ :

$$(\widehat{w}, \widehat{z}) \stackrel{d}{=} (\Lambda(w + sZ), \Lambda(z - sZ)).$$

For any fixed $\Lambda = \lambda$, the conditional distribution is

$$(\widehat{w}, \widehat{z}) \big|_{\Lambda=\lambda} = (\lambda(w + sZ), \lambda(z - sZ)), \quad Z \sim \mathcal{N}(0, 1).$$

Hence $(\widehat{w}, \widehat{z}) \big|_{\Lambda=\lambda}$ is bivariate normal with mean $(\lambda w, \lambda z)$, marginal variances $\lambda^2 s^2$, and correlation -1 . Conditioning on Λ therefore reduces the randomness to the single standard normal Z . For any measurable function $h : \mathbb{R}^2 \rightarrow \mathbb{R}$,

$$\mathbb{E}[h(\widehat{w}, \widehat{z})] = \mathbb{E}_\Lambda \mathbb{E}_Z[h(\Lambda(w + sZ), \Lambda(z - sZ))], \quad Z \sim \mathcal{N}(0, 1) \text{ and } Z \perp\!\!\!\perp \Lambda.$$

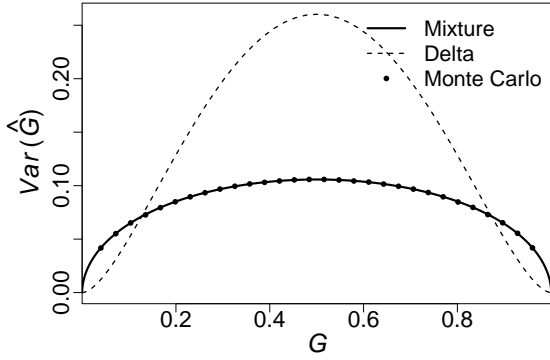
In other words, integrals with respect to the joint distribution of $(\widehat{w}, \widehat{z})$ reduce to a one-dimensional inner expectation over Z and a one-dimensional outer expectation over Λ . In particular, for subsequent calculations define, for $k = 1, 2$,

$$\mathcal{M}_k(\lambda; w, z) := \mathbb{E}_Z \left[G(\lambda(w + sZ), \lambda(z - sZ))^k \right], \quad \lambda > 0.$$

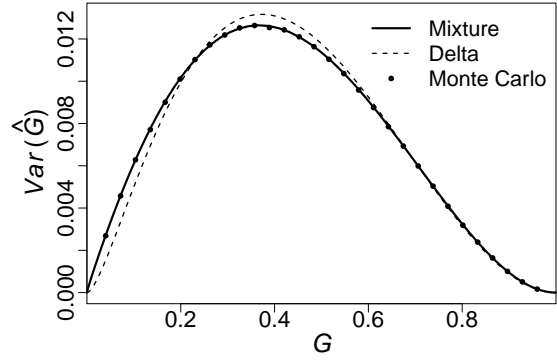
Then the unconditional mean and variance of $\widehat{G} := G(\widehat{w}, \widehat{z})$ are

$$\mathbb{E}[\widehat{G}] = \mathbb{E}_\Lambda[\mathcal{M}_1(\Lambda; w, z)], \quad \text{Var}(\widehat{G}) = \mathbb{E}_\Lambda[\mathcal{M}_2(\Lambda; w, z)] - (\mathbb{E}_\Lambda[\mathcal{M}_1(\Lambda; w, z)])^2.$$

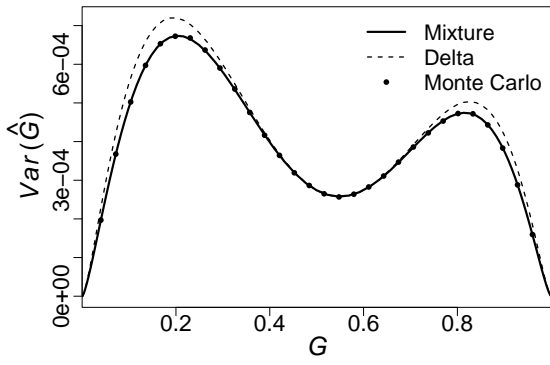
These representations are numerically stable and agree well with Monte Carlo simulations across a broad range of (w, z) values (Fig. S7.1).



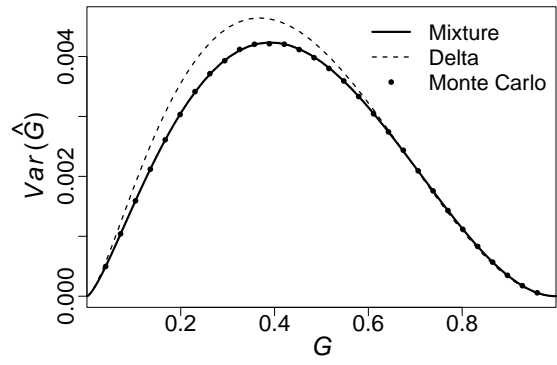
(a) $z = 20, t^* = 100$ (central $z > 0$ regime)



(b) $z = -5, t^* = 100$ (negative-tail regime)



(c) $z = 20, t^* = 0.1$ ($k < 1$, two-hump structure)



(d) $z = -5, t^* = 0.1$ ($k < 1$, single-peak)

Figure S7.1: Variance of the extinction-probability estimator $\text{Var}(\hat{G})$ as a function of the true extinction probability G . Each curve fixes z and varies w to sweep $G(w, z)$ over $(0, 1)$. Solid line: mixture evaluation; dashed line: delta method; dots: Monte Carlo simulations ($n = 120,000$). Mixture and Monte Carlo curves nearly coincide, representing the true finite-sample variance. (a,b): $t^* = 100$; (a) central $z > 0$ regime, (b) negative-tail regime. (c,d): $t^* = 0.1$ with $k < 1$; (c) $z > 0$ shows a two-hump structure, (d) $z < 0$ remains single-peaked. The delta method overestimates variance near the center for $z > 0$ (finite- q effect).

The case $z > 0$. When z is moderately large and positive (formally $z \rightarrow \infty$), the second term in $G(w, z)$ is exponentially small, so $\hat{G} \simeq \Phi(-\hat{w})$ and the inner expectation is one-dimensional in closed form:

$$\mathcal{M}_1(\lambda; w, z) \simeq \mathbb{E}_Z[\Phi(-\lambda(w + sZ))] = \Phi\left(\frac{-\lambda w}{\sqrt{1 + \lambda^2 s^2}}\right),$$

$$\mathcal{M}_2(\lambda; w, z) \simeq \mathbb{E}_Z[\Phi(-\lambda(w + sZ))^2] = \Phi_2(a(\lambda), a(\lambda); \varrho(\lambda)),$$

with

$$a(\lambda) = \frac{-\lambda w}{\sqrt{1 + \lambda^2 s^2}}, \quad \varrho(\lambda) = \frac{\lambda^2 s^2}{1 + \lambda^2 s^2},$$

and $\Phi_2(\cdot, \cdot; \varrho)$ the standard bivariate normal cdf with correlation ϱ . Therefore

$$\text{Var}_{z>0}(\widehat{G}) \simeq \mathbb{E}_\Lambda[\Phi_2(a(\Lambda), a(\Lambda); \varrho(\Lambda))] - \left(\mathbb{E}_\Lambda[\Phi(a(\Lambda))]\right)^2,$$

and the corresponding Wald half-width is

$$h_G^{\text{mix}}(w; z > 0) = z_{1-\alpha/2} \sqrt{\text{Var}_{z>0}(\widehat{G})}.$$

As $q \rightarrow \infty$ with t_q fixed, one has $\Lambda \rightarrow 1$ in probability and $s = \sqrt{t^*/t_q}$ fixed, so $a(\Lambda) \rightarrow -w/\sqrt{1 + s^2}$ and $\varrho(\Lambda) \rightarrow s^2/(1 + s^2)$. In this limit the variance reduces to the delta-method expression,

$$\text{Var}_{z>0}(\widehat{G}) = \phi(w)^2 \Sigma_{11} + o(1), \quad (q \rightarrow \infty).$$

where $\Sigma_{11} = c(q) (k + w^2)$ from (S7.1). Using the identity $c(q) k(q, t_q, t^*) = \frac{q}{q-3} \frac{t^*}{t_q}$,

$$\Sigma_{11} = c(q) \{k + w^2\} = c(q)k + c(q)w^2 \longrightarrow \frac{t^*}{t_q} = s^2 \quad (q \rightarrow \infty, t_q \text{ fixed}),$$

since $c(q) \rightarrow 0$ and $\frac{q}{q-3} \rightarrow 1$. Therefore, increasing q with fixed t_q does not reduce the width below the plateau

$$h_G^{\text{mix}}(w; z > 0, q \rightarrow \infty) \simeq z_{1-\alpha/2} \phi(w) \sqrt{\frac{t^*}{t_q}}.$$

$\text{Var}_{z>0}(\widehat{G})$ is an even function of w (by the symmetry $Z \mapsto -Z$), decays to zero as $|w| \rightarrow \infty$, and attains its maximum at $w = 0$ (so $G \simeq 0.5$). At the symmetry point $w = 0$ one has

$$\text{Var}_{z>0}(\widehat{G}) \Big|_{w=0} = \frac{1}{2\pi} \mathbb{E}_\Lambda \left[\arcsin \left(\frac{\Lambda^2 s^2}{1 + \Lambda^2 s^2} \right) \right] \longrightarrow \frac{1}{2\pi} \arcsin \left(\frac{s^2}{1 + s^2} \right) \quad (q \rightarrow \infty).$$

In particular, if $s^2 = 1$ (i.e., $t^* = t_q$), the limit equals $1/12$.

S7.4 Dependence on growth rate and environmental variance

For fixed (μ, x_d, t^*) ,

$$w^2 + z^2 = \frac{C^2}{\sigma^2}, \quad C^2 = \frac{2((\mu t^*)^2 + x_d^2)}{t^*}.$$

Hence iso- σ^2 contours are concentric circles centered at the origin in the (w, z) plane. Varying σ moves (w, z) radially with constant polar angle $\arctan(z_0/w_0)$, where $w_0 = (\mu t^* + x_d)/\sqrt{t^*}$ and $z_0 = (-\mu t^* + x_d)/\sqrt{t^*}$. As σ increases, (w, z) approaches the origin and the CI width grows, but the growth saturates at a plateau governed by (q, t_q) with scale $\sqrt{t^*/t_q}$. As σ decreases, (w, z) moves outward and G approaches 0 or 1, which drives the CI to shrink.

The qualitative split by the sign of μ follows from the boundary $w = z$. For $\mu < 0$, the locus $w = 0$ (equivalently $-\mu t^* = x_d$) marks a band of maximal uncertainty. As $\sigma \downarrow 0$ with (μ, x_d, t^*) fixed, write $w = w_0/\sigma$ and $z = z_0/\sigma$. If $z > 0$ (that is, $z_0 > 0$) then

$$G(w, z) \simeq \Phi(-w) \sim \frac{\phi(w)}{w} = O\left(\sigma e^{-w_0^2/(2\sigma^2)}\right).$$

If $z < 0$ (with $w + z > 0$) then

$$G(w, z) \simeq \exp\left(\frac{z^2 - w^2}{2}\right) = \exp\left(-\frac{w_0^2 - z_0^2}{2\sigma^2}\right).$$

Thus, away from the $w = 0$ ray, the CI width shrinks at rate $\exp(-\text{const}/\sigma^2)$ until it reaches the data-limited plateau of order $\sqrt{t^*/t_q}$. On the $w = 0$ ray (reachable only if $\mu = -x_d/t^*$), $G \rightarrow 1/2$ as $\sigma \downarrow 0$ and the CI remains maximal.

S7.5 Summary

The delta method provides a general analytic framework, cleanly separating data and model contributions and describing asymptotic dependence across regimes. The mixture representation, however, yields sharper results for finite q and is particularly powerful in the region $z > 0$, where the extinction probability reduces to a one-dimensional form and the distribution of \widehat{G} is available in semi-exact mixture form. In the central region, mixture calculations reveal that the delta method exaggerates the variance, while in the high-drift tail the delta method captures the exponential decay of the confidence-interval width. Together these approaches offer both interpretability and accuracy across the (w, z) plane.

From the standpoint of data dependence, the two methods highlight complementary roles of sample size (minus one) q and observation span t_q . Although $c(q) \sim 1/q$, the identity $c(q)k(q, t_q, t^*) = \frac{q}{q-3} \frac{t^*}{t_q}$ implies that, with t_q fixed, the leading entries of Σ converge to $s^2 = t^*/t_q$. Hence the width does not keep shrinking with q ; it plateaus at order $\sqrt{t^*/t_q}$. In the mixture representation, the random scale Λ captures the extra finite- q variability and vanishes as $q \rightarrow \infty$, while the rescaling factor $s = \sqrt{t^*/t_q}$ makes explicit how extending t_q reduces uncertainty. Thus q controls replication-driven precision, and t_q controls the per-observation signal-to-noise ratio; together they explain both the plateau (for fixed t_q as $q \rightarrow \infty$) and the substantial gains from increasing t_q .

Appendix S8. Table: Extinction probability and CI width versus time horizon t^* for $\mu < 0$ and $\mu > 0$ examples

Table S8.1: Representative examples of extinction probability and 95% CI width versus the time horizon t^* . The $\mu < 0$ case ($\mu = -0.058925$, $\sigma = 0.116939$, $x_d = 12.64433$; path crosses $w = 0$) contrasts with the $\mu > 0$ case ($\mu = 0.10$, $\sigma = 0.20$, $x_d = 13$; path does not cross $w = 0$). Here $q = t_q = 63$. G denotes the point estimate and “CI width” the two-sided interval width (the w - z method).

t^*	$\mu < 0$ (crosses $w = 0$)		$\mu > 0$ (does not cross $w = 0$)	
	G	CI width	G	CI width
25.5	1.87×10^{-79}	3.16×10^{-52}	2.13×10^{-53}	8.62×10^{-35}
42.5	1.91×10^{-40}	2.87×10^{-25}	8.64×10^{-40}	8.15×10^{-25}
100	5.32×10^{-9}	1.38×10^{-3}	4.60×10^{-30}	3.59×10^{-16}
250	0.88	9.97×10^{-1}	5.90×10^{-29}	4.16×10^{-13}
500	$1 - 3.74 \times 10^{-11}$	2.04×10^{-1}	5.90×10^{-29}	6.64×10^{-13}
1000	$1 - 1.08 \times 10^{-36}$	5.91×10^{-6}	5.90×10^{-29}	6.21×10^{-13}

Appendix S9. Determination of the required observation span

The numerical analysis in Subsection 4.8 rests on an explicit definition of the *required observation span*. Here the time horizon t^* is fixed in advance, while the observation span t_q is determined by the sampling design. A time series of population size with $q+1$ observations at times $t_i = i$ ($i = 0, \dots, q$) is considered under unit-interval, equally spaced sampling; hence the observation span t_q equals the number of increments q . Given a true extinction probability $P = G(w, z)$ and a prescribed confidence level $1 - \alpha$, the required span t_q is defined as the smallest integer such that the upper confidence bound of $G(w, z)$ falls below a management threshold G_{target} :

$$G_{\text{upper}}(t_q; w, z, \alpha) \leq G_{\text{target}}. \tag{S9.1}$$

To specify G_{upper} , note that the rescaled estimators \hat{w}, \hat{z} follow noncentral- t distributions (see Subsection 4.2):

$$\hat{w} \sqrt{\frac{t_q - 1}{t^*}} \sim t(\delta_w, t_q - 1), \quad \hat{z} \sqrt{\frac{t_q - 1}{t^*}} \sim t(\delta_z, t_q - 1), \tag{S9.2}$$

with noncentrality parameters

$$\delta_w = w\sqrt{\frac{t_q}{t^*}}, \quad \delta_z = z\sqrt{\frac{t_q}{t^*}}. \quad (\text{S9.3})$$

Let $\nu = t_q - 1$ and let $F_{t_\nu(\delta)}(\cdot)$ denote the CDF of the noncentral- t distribution with degrees of freedom ν and noncentrality parameter δ . Define $(\delta_{\text{low}}, \delta_{\text{high}})$ implicitly by

$$F_{t_\nu(\delta_{\text{low}})}\left(\sqrt{\frac{\nu}{t^*}} w\right) = 1 - \frac{\alpha}{2}, \quad (\text{S9.4})$$

$$F_{t_\nu(\delta_{\text{high}})}\left(\sqrt{\frac{\nu}{t^*}} z\right) = \frac{\alpha}{2}. \quad (\text{S9.5})$$

Let (w_L, z_U) be the parameter values induced by $(\delta_{\text{low}}, \delta_{\text{high}})$ via (S9.3). Because G decreases strictly in both arguments when $w + z > 0$ (Appendix S2), the upper bound is

$$G_{\text{upper}}(t_q; w, z, \alpha) = G(w_L, z_U).$$

The required observation span is then

$$t_q^* = \min\left\{t_q \in \mathbb{N} : G_{\text{upper}}(t_q; w, z, \alpha) \leq G_{\text{target}}\right\}. \quad (\text{S9.6})$$

For the numerical results in Subsection 4.8, the horizon was set to $t^* = 100$, the confidence level to $1 - \alpha = 0.95$, and the management threshold to $G_{\text{target}} = 0.1$. Equation (S9.6) was then solved across a range of true extinction probabilities $P = G(w, z)$, with z fixed and w chosen to match the desired P .

Appendix S10. Eel Harvests by Prefectures in Japan: Seed and Inland Fisheries

This appendix provides the full data background and extended methodological details that underpin the main-text analyses. It consolidates (i) data source descriptions and compilation notes, (ii) the relationship between catch and CPUE for glass eels, (iii) conversion of catch weight to numbers of individuals, and (iv) prefectural harvest summaries and figures.

S10.1 Fisheries statistics

Hakoyama *et al.* (2016) compiled a comprehensive historical dataset of Japanese fisheries statistics related to the Japanese eel, covering the period from 1894 onward. Key variables include the weight of eels harvested, the weight and number of seeds used for aquaculture, the number of eels stocked, and counts of management units involved in eel fisheries. These variables are reported at multiple spatial levels (sites such as rivers and lakes, prefectures, inland/coastal domains, and national totals). For recent

years and for certain prefectural series (e.g., Shizuoka), I also consulted the *Annual Reports of Catch Statistics on Fishery and Aquaculture in Japan*, the Annual Reports of the Shizuoka Prefectural Fisheries Experiment Station, and the prefectural bulletin *Hamana*; details are provided in the Data availability statement.

Seed-catch statistics differ between coastal and inland waters. In coastal waters, glass eels predominate, and reporting was intermittent in several major producing prefectures. The pronounced spike in the 1960s coincides with such intermittency (notably in Ibaraki), suggesting that compilation practices may have affected interannual comparability. In inland waters, seed statistics include both glass eels and elvers and show more consistent numerical coverage; in the 1960s–1970s, large elver catches were reported from the Tone River.

Compilation and reporting practices, such as unusually large elver catches in earlier decades or coastal series dominated by intermittent reports from Ibaraki, can influence trends, leading to overestimation of decline rates and hence extinction risk. However, I retained the original seed series to ensure a precautionary assessment that does not understate extinction risk. This approach also facilitates direct comparison with the abundance-based evaluation under IUCN Criterion A, highlighting its methodological contrast with Criterion E. Details on prefectural patterns and potential aggregation issues are provided below.

S10.2 Glass eel indices: catch and CPUE analysis

Glass eel indices in coastal waters are represented by catch and CPUE (catch per unit effort). Because CPUE is available only for limited years, mainly from the Eel Culture Research Council reports (1977–1997) and with gaps elsewhere, catch serves as the primary index for long time spans. Where overlapping years exist, aggregate data from major prefectures show that catch trends closely parallel CPUE, consistent with relatively stable fishing effort over time. Shizuoka Prefecture, which ranks second in total coastal harvest and has the only uninterrupted coastal catch series, exemplifies this relationship. In Shizuoka, catch closely tracks CPUE in the overlapping years, supporting the use of catch as an abundance index when CPUE is unavailable (Fig. S10.1).

Although not shown here, CPUE series for glass eels over the past two decades are strongly correlated among prefectures, indicating broad interannual synchrony in availability (Hakoyama et al., in preparation). This synchrony supports the use of regional series, such as Shizuoka, as representative of broader coastal trends.

S10.3 Conversion of catch weight to numbers of individuals

Catch weight data were converted to estimated numbers of individuals by dividing by the mean body weight specific to each developmental stage: 0.2 g for glass eels, 12.5 g for elvers, and 200 g for yellow eels.

S10.4 Prefectural harvest summaries and figures

Fishery categories. Within the seed-fishery category, coastal fisheries correspond mainly to glass eels, whereas inland seed fisheries cover both glass eels and elvers. Historically, large elver catches were reported in some inland series, but in recent decades glass eels have predominated. In addition, inland eel fisheries target yellow and silver eels.

Coding of special symbols. The original tables use three non-numeric symbols: a dash (–) denotes *no catch / no response* (the sources do not distinguish these); “*x*” denotes *confidential*; and “:” denotes *prefecture unspecified*. In the heatmaps these symbols are overlaid as shaded cells so their occurrence can be evaluated alongside numeric values on the \log_{10} scale.

Coastal seed fisheries (glass eel). Coastal series contain frequent entries marked as no catch or no response, including in prefectures with high average harvest. This pattern suggests that many of these cases likely reflect non-response rather than confirmed zero catch. Shizuoka is the only coastal prefecture with a continuous numeric series throughout the period and is among the top producers. By contrast, several major producers, notably Ibaraki, exhibit intermittent reporting during key periods such as the 1960s, increasing the prevalence of missing values in years when catches were likely positive.

Inland seed fisheries (glass eel and elver). Inland series also contain missing-value entries, but their distribution differs from the coastal case. Prefectures with high average harvest tend to show fewer such gaps, whereas a subset of prefectures report almost exclusively missing values over time, consistent with sustained zero catch or the absence of target fisheries. Overall, inland seed-fishery data provide more complete numeric coverage than coastal data.

National versus prefectural totals (seed fisheries). The sum of prefectural reports broadly tracks the national totals, indicating consistency in most years. However, if missing entries represent non-response rather than true zero catch, prefectural sums would underestimate actual harvests. This potential aggregation bias is of greatest concern for coastal data, where gaps are common even in large-producing prefectures; in particular, Ibaraki’s reporting pattern raises concern that substantial catches may be missing from the prefectural tables.

Inland eel fisheries (yellow and silver). Inland harvests of yellow and silver eels are available for 1957–2020 and show high continuity, with very few missing values or symbol-coded entries. The national series peaks in the late 1960s at over 3,000 t and declines steadily thereafter to a few hundred tonnes in recent years. At the prefectural

level, early records indicate widespread harvest across many regions, while later decades show contraction toward fewer producing prefectures. These continuous inland series provide a reliable indicator of long-term decline in exploited inland eel stocks.

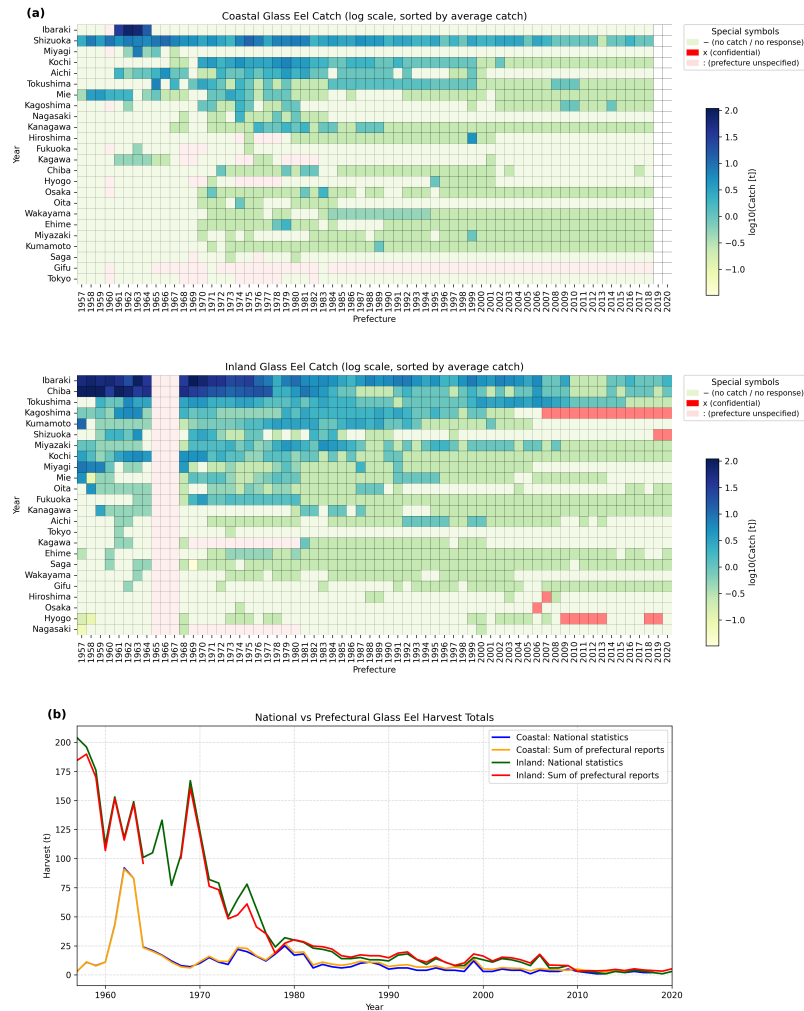


Figure S10.1: Seed-fishery harvests of glass eels and elvers by prefecture in Japan (coastal: 1957–2018; inland: 1957–2020), compiled from Hakoyama *et al.* (2016) and the Annual Reports of Catch Statistics on Fishery and Aquaculture in Japan. (a) Heatmaps of annual catch by prefecture on a \log_{10} scale; columns are sorted by average harvest and special symbols from the sources are retained as overlaid cells. (b) National totals versus the sum of prefectural reports.

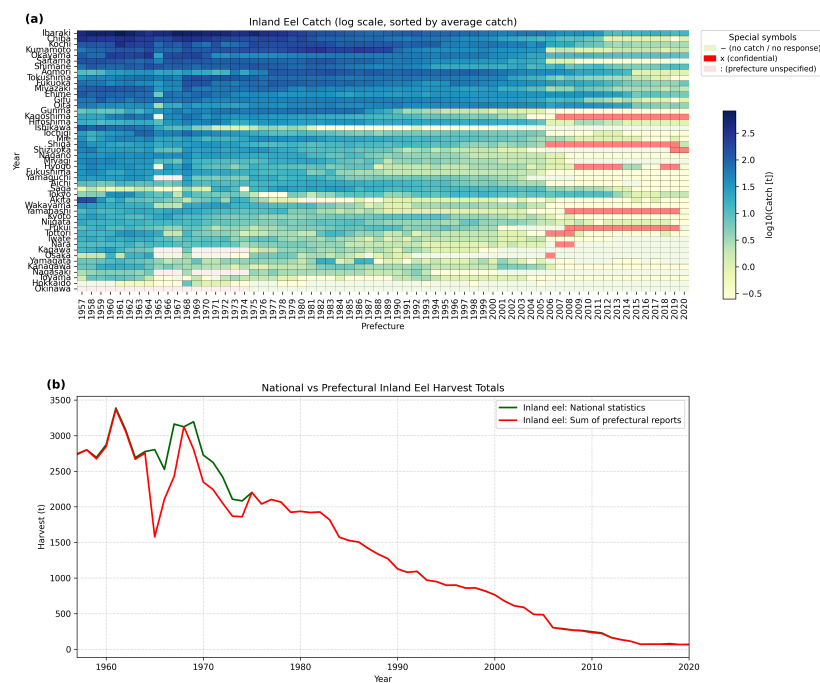


Figure S10.2: Inland eel fisheries (yellow and silver eels), 1957–2020. (a) \log_{10} -scaled heatmap of annual harvest by prefecture; columns sorted by average harvest. (b) National harvest totals through time. Data from Hakoyama *et al.* (2016) and the Annual Reports of Catch Statistics on Fishery and Aquaculture in Japan.

Appendix S11. Criterion E thresholds and generation time

S11.1 Criterion E thresholds and evaluation horizons

The IUCN Red List includes Criterion E, which relies on a quantitative analysis of extinction probability (IUCN, 2012). Under this criterion, a species is categorized as *Critically Endangered* (CR) if the probability of extinction in the wild is at least 50% within 10 years or three generations, whichever is longer, up to a maximum of 100 years. A species qualifies as *Endangered* (EN) if the probability of extinction is at least 20% within 20 years or five generations, whichever is longer, with the same 100-year maximum. For the *Vulnerable* (VU) category, the threshold is a probability of at least 10% within 100 years.

Given the generation time estimated below, three generations equal 25.5 years and five generations equal 42.5 years for the Japanese eel. Extinction probabilities are therefore evaluated over 25.5, 42.5, and 100 years in accordance with Criterion E.

S11.2 Generation time estimation

Generation time is a key demographic parameter with several alternative definitions. In age-structured models, one common measure is the mean age of the parents of the offspring produced by a cohort over its lifetime (Caswell, 2001; Coale, 1972). This cohort-based measure is equivalent to the average parental age weighted by fertility, and in a stationary population it coincides with the mean parental age at the stable age distribution. Such measures are conceptually distinct from definitions based on the time required for a population to increase by its net reproductive rate, but they generally provide consistent values when survival is high and growth rates are near unity.

For the Japanese eel *Anguilla japonica*, generation time is complicated by the pronounced difference in maturation age between sexes and by geographic variation in growth. Males typically mature between 4 and 10 years and females between 3 and 17 years, with mean estimates around 7–10 years depending on locality (Kotake *et al.*, 2005; 2007; Yokouchi *et al.*, 2009). Comparable studies on the European eel *A. anguilla* have demonstrated geographic variation in both mean age and length at metamorphosis, reflecting fixed developmental trajectories expressed under different environmental conditions rather than adaptive plasticity (Vøllestad, 1992). These findings suggest that geographic heterogeneity in age at silvering is to be expected also for the Japanese eel, and that estimates of generation time should integrate across sites to obtain a representative mean.

In this study, I estimated generation time from mean ages of female silver eels collected at multiple sites, weighted by sample size, with an additional ≈ 0.5 years to account for the estimated migration period from continental waters to the spawning grounds. The weighted mean age across sites was ≈ 8 years; adding ≈ 0.5 years for migration gives ≈ 8.5 years. For Criterion E calculations, a generation time of 8.5 years was adopted, yielding evaluation horizons of 25.5, 42.5, and 100 years. The underlying data are summarized in Table S11.1.

Table S11.1: Mean age of female silver eels at different locations.

Location	Period	Mean age (yr)	n	Source
Kaoping River, Taiwan	1998–2003	5.95	42	Han <i>et al.</i> (2009)
Amakusa Islands, Japan	–	7.80	19	Kotake <i>et al.</i> (2007)
Mikawa Bay, Japan	–	8.10	84	Kotake <i>et al.</i> (2007)
Sanriku Coast, Japan	–	8.80	5	Kotake <i>et al.</i> (2007)
Mikawa Bay, Japan	Oct–Dec	7.90	132	Kotake <i>et al.</i> (2005)
Hamana Lake, Japan	2003–2007	9.90	78	Yokouchi <i>et al.</i> (2009)